

# Effects of Atwood and Reynolds numbers on the evolution of buoyancy-driven homogeneous variable-density turbulence

Denis Aslangil<sup>1,2,†</sup>, Daniel Livescu<sup>2</sup> and Arindam Banerjee<sup>1</sup>

<sup>1</sup>Department of Mechanical Engineering and Mechanics, Lehigh University, Bethlehem, PA 18015, USA

<sup>2</sup>Los Alamos National Laboratory, Los Alamos, NM 87545, USA

(Received 14 November 2019; revised 14 March 2020; accepted 27 March 2020)

The evolution of buoyancy-driven homogeneous variable-density turbulence (HVDT) at Atwood numbers up to 0.75 and large Reynolds numbers is studied by using high-resolution direct numerical simulations. To help understand the highly non-equilibrium nature of buoyancy-driven HVDT, the flow evolution is divided into four different regimes based on the behaviour of turbulent kinetic energy derivatives. The results show that each regime has a unique type of dependence on both Atwood and Reynolds numbers. It is found that the local statistics of the flow based on the flow composition are more sensitive to Atwood and Reynolds numbers compared to those based on the entire flow. It is also observed that, at higher Atwood numbers, different flow features reach their asymptotic Reynolds-number behaviour at different times. The energy spectrum defined based on the Favre fluctuations momentum has less large-scale contamination from viscous effects for variable-density flows with constant properties, compared to other forms used previously. The evolution of the energy spectrum highlights distinct dynamical features of the four flow regimes. Thus, the slope of the energy spectrum at intermediate to large scales evolves from  $-7/3$  to  $-1$ , as a function of the production-to-dissipation ratio. The classical Kolmogorov spectrum emerges at intermediate to high scales at the highest Reynolds numbers examined, after the turbulence starts to decay. Finally, the similarities and differences between buoyancy-driven HVDT and the more conventional stationary turbulence are discussed and new strategies and tools for analysis are proposed.

**Key words:** turbulent mixing, homogeneous turbulence, buoyancy-driven instability

---

## 1. Introduction

The mixing of two or more miscible fluids with different densities (or molar masses) is of fundamental interest due to the occurrence of such mixing in atmospheric and oceanic flows (Adkins, McIntyre & Schrag 2002; Molchanov 2004; Wunsch & Ferrari 2004), supernova formation (Colgate & White 1966; Gull 1975; Nouri, Givi & Livescu 2019), combustion applications in ramjet engines (Givi 1989; Clemens

† Email address for correspondence: [denis.aslangil@gmail.com](mailto:denis.aslangil@gmail.com)

& Mungal 1995; Sellers & Chandra 1997) and high-energy-density processes like inertial confinement fusion (Lindl 1995, 1998; Nakai & Takabe 1996; Nakai & Mima 2004). These flows are traditionally referred to as variable-density (VD) flows in the scientific literature. Unlike incompressible single-fluid flows, the velocity field in VD flows is tightly coupled to the density field and is not divergence-free, even in the incompressible limit. The VD mixing process is directly related to flow dynamics and plays a vital role in the flow evolution, as compositional changes lead to significant effects on both the mixing behaviour and the resultant turbulence structure (Livescu & Ristorcelli 2007; Chung & Pullin 2010; Gat *et al.* 2017; Rao, Caulfield & Gibbon 2017; Aslangil, Livescu & Banerjee 2019, 2020; Livescu 2020). Here, we investigate buoyancy-driven homogeneous variable-density turbulence (HVDT) by high-resolution direct numerical simulations (DNS) in triply periodic domain sizes up to  $2048^3$ .

Introduced by Batchelor, Canuto & Chasnov (1992) to investigate buoyancy-driven turbulence under Boussinesq approximation, homogeneous buoyancy-driven turbulence is a canonical fluid flow problem; the presence of triply periodic boundaries eliminates the inhomogeneities that may arise in the flow due to the mixing-layer edge and/or wall effects (Batchelor *et al.* 1992; Sandoval 1995; Livescu & Ristorcelli 2007). Initial large pure-fluid regions with different densities start to move in opposite directions when acceleration is applied to the domain. The main turbulent kinetic energy production mechanism is through the product of the mean pressure gradient and the mass flux (Livescu & Ristorcelli 2007). At the same time, vorticity is produced through the baroclinic mechanism due to misalignment of pressure and density gradients. The non-dimensional number representing the density contrast between the two fluids is the Atwood number,

$$A = \frac{\rho_2 - \rho_1}{\rho_2 + \rho_1} \Rightarrow \frac{\rho_2}{\rho_1} = \frac{1 + A}{1 - A}, \quad (1.1)$$

where  $\rho_1$  and  $\rho_2$  are the densities of the light and heavy fluids, respectively. This study covers a broad range of non-dimensional density ratios from 1.105 : 1 to 7 : 1, which correspond to Atwood-number values from 0.05 to 0.75, and spans both the traditional Boussinesq case ( $A = 0.05$ ) and the strongly non-Boussinesq case ( $A = 0.5$  and 0.75).

HVDT is of interest to the turbulence community also because it mimics the core of the mixing layer formed by the acceleration-driven Rayleigh–Taylor instability (RTI) (Rayleigh 1884; Taylor 1950) and the shock-driven Richtmyer–Meshkov instability (RMI) (Richtmyer 1960; Meshkov 1969). In addition, it has some similarities with VD jet flows (Charonko & Prestridge 2017) and VD shear (mixing) layers (Schwarzkopf *et al.* 2016; Almagro, García-Villalba & Flores 2017; Baltzer & Livescu 2020). In RTI, VD mixing occurs between light and heavy fluids in the presence of an acceleration field, where the heavy fluid sits on top of the light fluid (Ristorcelli & Clark 2004; Banerjee & Andrews 2009). The generality of the HVDT findings was later confirmed by comparisons with the classical RTI studies by Livescu *et al.* (2009, 2010). Higher-Atwood-number simulations by Livescu, Wei & Petersen (2011),  $A$  up to 0.75, and RTI gas-channel experiments by Banerjee, Kraft & Andrews (2010),  $A$  up to 0.6, and by Akula & Ranjan (2016),  $A$  up to 0.73, also confirm those findings. An important aspect of these flows is the heavy-light fluid mixing asymmetry (Livescu & Ristorcelli 2008, 2009; Livescu 2013), manifested, for example, in different penetration levels of light and heavy fluids, indicating different turbulent features of the flow for the bubble side (mostly composed of light fluid) and spike side (mostly composed of heavier fluid). In some important applications, like inertial confinement

fusion, blast waves and astrophysical flows such as Type Ia supernovae, RTI is driven by time-varying accelerations. Such effects have been studied in the context of RTI by Dimonte & Schneider (1996), Livescu *et al.* (2011), Livescu & Wei (2012), Ramaprabhu, Karkhanis & Lawrie (2013) and Aslangil, Banerjee & Lawrie (2016). HVDT has certain connections with RTI under variable acceleration as the HVDT evolution has unsteady turbulent kinetic energy ( $E_{TKE}$ ) behaviour with  $dE_{TKE}/dt$  and/or  $d^2E_{TKE}/dt^2$  phases which are reminiscent of the RTI problem with  $dg_i/dt \neq 0$ . Another application of interest is VD RMI; the flow is driven by one or more shocks that pass through the interface between light and heavy fluids (Brouillette 2002; Schilling, Latini & Don 2007; Schilling & Latini 2010; Zhou 2017*a,b*). In RMI, shock-generated turbulence decays, while the fluids molecularly mix (Nishihara *et al.* 2010; Bailie *et al.* 2012). This behaviour has similarities with the late-time decay of HVDT where the buoyancy forces weaken and buoyancy-generated VD turbulence decays. The late-time decay stage of buoyancy-driven HVDT, where the VD effects are minimal, also has some similarities with buoyancy-driven Rayleigh–Beñard convection, which occurs between two plates such that the bottom plate is heated (Getling 1998; Ahlers, Grossmann & Lohse 2009).

Several studies have used the homogeneous configuration to investigate VD effects on buoyancy-driven turbulence (Sandoval 1995; Sandoval, Clark & Riley 1997; Livescu & Ristorcelli 2007, 2008). Sandoval (1995) and Sandoval *et al.* (1997) studied VD dynamics of the buoyancy-driven turbulence at fairly low Reynolds numbers (domain size  $\approx 128^3$ ). Livescu & Ristorcelli (2007, 2008) used the homogeneous configuration to investigate VD effects on buoyancy-driven turbulence and turbulent mixing with density ratios up to 3 : 1 and higher Reynolds numbers. Chung & Pullin (2010) studied VD mixing in a stationary HVDT configuration, where the flow is continuously fed pure heavy fluid from the top and pure light fluid from the bottom of the domain, leading to a stationary state. More recently, Gat *et al.* (2017) numerically studied VD turbulence in vertical fluid columns with different densities that are moving in opposite directions due to the presence of an acceleration field. In their study, the buoyancy forces generate a VD shear layer, while the two fluids are molecularly mixing.

### 1.1. Highlights of this study

In this paper, buoyancy-driven HVDT is investigated by high-resolution DNS, up to domain sizes of  $2048^3$ , and covers a broad range of density ratios from 1.105 : 1 (corresponding to Atwood-number value of 0.05, which is close to the traditional Boussinesq case) to 7 : 1 (corresponding to Atwood-number value of 0.75). The simulations significantly extend the range of parameters from Livescu & Ristorcelli (2007, 2008) in terms of both the Reynolds and Atwood numbers. This HVDT flow provides unique challenges for turbulence modelling compared to, for example, the more complex RTI because it does not reach a self-similar stage. Owing to the unsteady nature of the mean variables, since turbulence undergoes a rapid initial increase in the kinetic energy followed by a buoyancy-mediated decay, the flow encompasses the generation, growth and decay of buoyancy-driven turbulence. Such a behaviour allows us to compare this canonical flow to a wide range of VD flow applications such as RTI under constant acceleration, RTI under time-varying acceleration, RMI, VD jets and VD shear layers.

To streamline the connection between the idealized HVDT flow and various applications, as well as to isolate specific physical behaviours, we have identified

four different regimes of the flow based on time derivatives of turbulence kinetic energy ( $E_{TKE}$ ). These regimes are named according to the growth/decay of  $E_{TKE}$  in the flow as follows:

- (I) explosive growth, when  $dE_{TKE}/dt > 0$ ,  $d^2E_{TKE}/dt^2 > 0$ ;
- (II) saturated growth, when  $dE_{TKE}/dt > 0$ ,  $d^2E_{TKE}/dt^2 < 0$ ;
- (III) fast decay, when  $dE_{TKE}/dt < 0$ ,  $d^2E_{TKE}/dt^2 < 0$ ; and
- (IV) gradual decay, when  $dE_{TKE}/dt < 0$ ,  $d^2E_{TKE}/dt^2 > 0$ .

Both high-Reynolds-number and large-density-ratio effects on buoyancy-driven HVDT, which add additional nonlinearities to the problem by causing significant asymmetries within the flow, are investigated. Unlike previous studies that mostly examined the global behaviour, we compare different regions in the flow by using conditional expectations to evaluate the asymmetric behaviour of density and velocity fields. In addition, the transport equation for the density–velocity joint mass density function (jMDF) is analysed. Such information can also be used in the context of modelling using probability density function (p.d.f) methods (Pope 1985). Furthermore, the energy conversion rates are compared for different  $A$  and turbulent Reynolds numbers during the growth regimes. Our largest-resolution simulations with domain sizes of  $1024^3$  and  $2048^3$  show that the results become converged with increasing Reynolds number. This allows us to comment on the notion of the mixing transition for VD turbulence. The last regime, gradual decay, exhibits long-time buoyancy-assisted turbulence decay, which is different from the traditional non-buoyant turbulence decay. The results show that the buoyancy-assisted  $E_{TKE}$  decay occurs at non-decaying turbulent Reynolds number. Finally, we suggest the Favre fluctuation momentum as a proper way of investigating the evolution of the energy spectra in variable-density turbulence (VDT), and the turbulence spectral evolution during the four flow regimes is characterized.

The rest of the paper is organized as follows. In §2, we first present the governing equations, computational approach and simulation cases. Next, we define some useful mathematical tools to analyse our flow. Then §3 presents the global evolution of the buoyancy-driven HVDT. Connections to applications such as RTI and RMI are also introduced in §3. The flow asymmetries during the four different regimes (I–IV) are discussed in §4; and §5 examines the spectral evolution of HVDT. Finally, §6 summarizes our findings, and discusses the main conclusions of the paper.

## 2. Problem formulation, simulation cases and tools to analyse the flow

Throughout the paper, the superscript  $*$  is used for instantaneous values; capital Roman letters or angle brackets are used for mean values; and lower-case Roman letters or primes are used for Reynolds fluctuations. The velocity decomposition in index notation is  $u_i^* = U_i + u_i$ , while the density decomposition is  $\rho^* = \bar{\rho} + \rho$ . Moreover, Favre (density-weighted) averaged values are denoted using tilde  $\tilde{\phantom{x}}$  and Favre fluctuations are denoted using double primes  $''$ , such that  $u_i^* = \tilde{U}_i + u_i''$ , with  $\tilde{U}_i = \langle \rho^* u_i^* \rangle / \bar{\rho}$ .

### 2.1. Governing equations

The governing equations describing the mixing of two fluids with different densities can be derived from the fully compressible Navier–Stokes equations with two miscible

fluids (species) with full diffusion and heat flux operators, as the infinite-speed-of-sound limit (Livescu 2013). In non-dimensional form, they can be written as (Cook & Dimotakis 2001; Livescu & Ristorcelli 2007)

$$\rho_{,t}^* + (\rho^* u_j^*)_{,j} = 0, \quad (2.1)$$

$$(\rho^* u_i^*)_{,t} + (\rho^* u_i^* u_j^*)_{,j} = -p_{,i}^* + \tau_{ij}^* + \frac{1}{Fr^2} \rho^* g_i, \quad (2.2)$$

where  $\rho^*$  is the density,  $u_i^*$  is the velocity in direction  $i$ ,  $p^*$  is the pressure,  $g_i$  is the gravity (acceleration) in direction  $i$ , and the stress tensor is assumed Newtonian,  $\tau_{ij}^* = (\rho^*/Re_0)(u_{i,j}^* + u_{j,i}^* - \frac{2}{3}u_{k,k}^* \delta_{ij})$ . In incompressible VD turbulence, the divergence of velocity is not zero due to the change in specific volume during mixing and can be written as

$$u_{j,j}^* = -\frac{1}{Re_0 Sc} \ln \rho_{,jj}^*. \quad (2.3)$$

This relation can also be derived either from the mass fraction transport equations or from the energy transport equation as the infinite-speed-of-sound limit (Livescu 2013). For the binary case, mass conservation for two fluids with constant densities,  $\rho_1$  and  $\rho_2$ , requires

$$\frac{1}{\rho^*} = \frac{Y_1^*}{\rho_1} + \frac{Y_2^*}{\rho_2}, \quad (2.4)$$

where  $Y_1$  and  $Y_2$  are the mass fractions of the two fluids. This relation also represents the infinite-speed-of-sound limit of the ideal gas equation of state for the mixture (Livescu 2013). Since  $Y_1^* + Y_2^* = 1$ , relation (2.4) becomes a diagnostic equation for mass fractions.

The non-dimensional parameters in (2.1)–(2.3) are the computational Reynolds number,  $Re_0$ , Schmidt number,  $Sc$ , and Froude number,  $Fr$ , defined as

$$Re_0 = \rho_0 L_0 U_0 / \mu_0, \quad (2.5)$$

$$Sc = \mu_0 / \rho_0 D_0, \quad (2.6)$$

$$Fr^2 = U_0^2 / g L_0, \quad (2.7)$$

where  $\rho_0 = (\rho_1 + \rho_2)/2$  is the reference density, and for the initial conditions in this paper it is equal to the mean density (calculated as the volumetric average  $\bar{\rho} = (1/\mathcal{V}) \int_{\mathcal{V}} \rho^* d\mathcal{V}$  due to the homogeneity of the flow),  $g$  is the magnitude of the acceleration field,  $\mu_0$  is the reference dynamic viscosity,  $D_0$  is the diffusion coefficient, and  $L_0$  and  $U_0$  are the reference length and velocity scales, respectively. For the cases investigated in this paper,  $D_0$  is constant, while the instantaneous dynamic viscosity,  $\mu^* = \mu_0 \rho^* / \rho_0 = \nu_0 \rho^*$ , where  $\nu_0$  is the reference kinematic viscosity and is constant (see table 1). This ensures that the instantaneous Schmidt number is uniform and constant during the flow evolution. For all cases considered,  $Sc = 1$ . The mixture rule implied by the instantaneous dynamic viscosity relation is  $1/\mu^* = Y_1^*/\mu_1 + Y_2^*/\mu_2$ , where  $\mu_1$  and  $\mu_2$  are the dynamic viscosities of the two fluids. Similarly, for all cases considered in the paper,  $Fr = 1$ .

As shown below, it is useful to further scale the results by the velocity scale  $U_r = \sqrt{A/Fr^2}$  and time scale  $t_r = \sqrt{Fr^2/A}$ , as some of the quantities discussed collapse with this scaling. The corresponding dimensional quantities are  $U_r^\dagger = U_r U_0 = \sqrt{AgL_0}$  and  $t_r^\dagger = t_r L_0 / U_0 = \sqrt{L_0 / Ag}$ . In the triply periodic case, there is no intrinsic length scale; however, to account for the initial fluid distribution and to facilitate

Cases	A	$Re_0$	$Re_{b0}$	$Re_{\lambda,max}$	Resolution
A1Re5	0.05	20 000	7014	490	2048 <sup>3</sup>
A1Re4*	0.05	10 000	3507	298	1024 <sup>3</sup>
A1Re3	0.05	4000	1403	139	512 <sup>3</sup>
A1Re1	0.05	1563	548	69	256 <sup>3</sup>
A2Re3	0.25	4000	3137	261	1024 <sup>3</sup>
A2Re1	0.25	1563	1225	120	512 <sup>3</sup>
A3Re2	0.5	3125	3466	236	1024 <sup>3</sup>
A3Re1	0.5	1563	1733	144	1024 <sup>3</sup>
A3Re0	0.5	556	616	62	512 <sup>3</sup>
A4Re2	0.75	3125	4245	191	2048 <sup>3</sup>
A4Re1	0.75	1563	2123	122	1024 <sup>3</sup>
A4Re0	0.75	556	755	58	512 <sup>3</sup>

TABLE 1. Parameters for the DNS cases. \*Similar results for this case, with a slightly different initialization, are available through the Johns Hopkins Turbulence Database (Livescu *et al.* 2014).

the comparison with other flows, such as RTI and RMI,  $L_0$  can be taken as the initial density integral scale. Using  $L_0$ ,  $U_r^\dagger$  and  $l_r^\dagger$  for non-dimensionalization changes the non-dimensional parameters in the governing equations to  $Fr^{\dagger 2} = A$  and  $Re_0^\dagger = Re_0 \sqrt{A/Fr^2} = \rho_0 L_0 \sqrt{AgL_0}/\mu_0$ .

In HVDT, due to the periodic boundary conditions, the pressure can only be determined up to a constant gradient. Thus, the mean pressure gradient needs to be specified. Similar to Livescu & Ristorcelli (2007, 2008), the mean pressure gradient is chosen to obtain a maximally unstable flow (understood as the time derivative of the mass flux attaining its maximum absolute value):

$$P_{,i} = \frac{1}{V} \left( \frac{1}{Fr^2} g_i - \langle vp_{,i} \rangle + \langle u_i u_{j,j} \rangle + \langle v \tau_{ij,j} \rangle \right), \quad (2.8)$$

where  $V$  is the mean specific volume ( $v^* = 1/\rho^* = V + v$ ). This also leads to  $U_i = 0$ ; hence, in this study  $u_i^* = u_i$ . This choice of  $P_{,i}$  is consistent with previous studies of HVDT by Sandoval *et al.* (1997), where similar arguments are used but under the Boussinesq approximation. Detailed derivations to this effect can be found in §2.2 of Livescu & Ristorcelli (2007). As noted in that 2007 paper, the choice of the maximally unstable flow sets the mean velocity to the value of zero; this is similar to observations by Cabot & Cook (2006) and Livescu *et al.* (2009) in the core region of the RTI, where  $P_{,i}$  is set by the non-periodic boundary conditions. Thus, this flow has significant similarities to the RTI, as explained in Livescu *et al.* (2009). The choice  $P_{,i} = 0$  has been made by Gat *et al.* (2017) in their acceleration-driven mixing-layer study. In that study, which had non-zero mean velocity, the vertical growth of the mixing layers is minimized, while the horizontal growth is maximized, which has analogies with vertical convection or differential heated cavities (see also Livescu 2020).

## 2.2. Computational approach and simulation cases

Equations (2.1) and (2.2), together with the divergence condition (2.3), are solved in a triply periodic domain of size  $(2\pi)^3$ , using the CFDNS code, as described in Livescu

& Ristorcelli (2007). The spatial derivatives are evaluated using Fourier transforms, and the time advancement is performed with the variable-time-step third-order Adams–Bashforth–Moulton scheme, coupled with a fractional-time method. To minimize the aliasing errors, the advection terms are written in the skew-symmetric form.

Table 1 lists the various cases that were chosen to investigate the influence of the Atwood and Reynolds numbers on HVDT. In the nomenclature chosen for the case names, the index following the first letter, A, varies from 1 to 4, denoting the Atwood numbers, 0.05, 0.25, 0.5 and 0.75, respectively. In addition, case names include the  $Re_0$  index from 0 to 5 corresponding to six different values of  $Re_0$  in increasing order, 556, 1563, 3125, 4000, 10 000 and 20 000, respectively. Also tabulated is a static buoyancy Reynolds number  $Re_{b0}$  defined as (Batchelor *et al.* 1992; Livescu & Ristorcelli 2007)  $Re_{b0} = Re_0 \sqrt{\mathcal{L}_\rho^3 A / Fr^2}$ , where  $\mathcal{L}_\rho$  is the initial density integral length scale. The Taylor Reynolds number is calculated from the turbulence Reynolds number,  $Re_t$ , using the isotropic turbulence formula  $Re_t = \sqrt{(20/3)Re_t}$ , where

$$Re_t = Re_0 \langle \rho^* u_i'' u_i'' \rangle^2 / (\bar{\rho} \epsilon), \quad (2.9)$$

and  $\epsilon = -\langle u_{i,j} \tau_{ij} \rangle$  is the dissipation in the turbulent kinetic energy equation.

The density field in all simulations is initialized as a Gaussian random field with top-hat energy spectrum between wavenumbers 3 and 5. After transforming into the real space, the negative values are assigned as 1, and the positive values are assigned as  $(1 + A)/(1 - A)$ ; the pure-fluid densities thus yield the desired Atwood number. To ensure that the mixing layer between the pure-fluid regions is captured on the grid, a Gaussian filter is used to smoothen the density field, thereby preserving the bounds. The width of the Gaussian filter is  $1.1\Delta x$  and is applied once for  $256^3$  and  $512^3$ , four times for  $1024^3$  (resulting in a total width of  $\approx 2.2\Delta x$ ), and 16 times for  $2048^3$  resolutions (resulting in a total width of  $\approx 4.4\Delta x$ ); the density integral length scale and mixing-state parameter (defined below) are similar for all cases.

After the initialization procedure, the non-dimensional initial density integral length scale, which is calculated from the resultant density spectra by

$$\mathcal{L}_\rho = 2\pi \int_0^\infty \frac{E_\rho(\mathcal{K})}{\mathcal{K}} d\mathcal{K} / \int_0^\infty E_\rho(\mathcal{K}) d\mathcal{K}, \quad (2.10)$$

is 1.3–1.4 for all cases. The initial mixing state is represented by a commonly used mixing-state parameter,  $\theta$  (Youngs 1991; Linden, Redondo & Youngs 1994), defined as

$$\theta = 1 - \frac{\langle \rho^2 \rangle}{(\bar{\rho} - \rho_1)(\rho_2 - \bar{\rho})}, \quad (2.11)$$

where  $\bar{\rho}$  is the mean density. The initial value of  $\theta$  is  $\theta_0 = 0.068$ – $0.07$  for the cases considered in table 1 except for the case A1Re1 for which  $\theta_0 = 0.14$ .

The non-dimensional acceleration field is  $g_i = (-1, 0, 0)$  and is gradually applied to the flow between  $t/t_r = 0$  and 0.1. A fifth-order polynomial equation is used to allow the flow to have a smooth transition from rest to the accelerated phase. This is especially important at high Atwood numbers, where exceedingly small time steps would otherwise be required at the initial times for accuracy. All simulations are well resolved, with  $\eta k_{max} > 2$  at all times during the flow evolution, except the A3Re2 case, for which  $\eta k_{max} > 1.7$ . Here,  $\eta = \{1/[Re_0^3(\epsilon/\rho_0)]\}^{1/4}$  is the Kolmogorov micro-scale, and  $k_{max} = \pi N/\mathcal{L} = N/2$  is the largest resolved wavenumber. All data presented from

the  $256^3$  resolution cases represent averages over 10 realizations, while data from  $512^3$  resolution cases represent averages over three realizations. The initial conditions for different realizations were generated using different random-number seeds. Because of the computational cost, cases with higher resolutions ( $1024^3$  and  $2048^3$ ) represent only one realization.

### 2.3. Energy budgets

To help describe the turbulence evolution, we define below the scalar energy (half density variance), the total and turbulent kinetic energies, as well as the potential energy, and discuss their transport equations.

#### 2.3.1. Scalar energy ( $E_\rho$ )

Here, the scalar energy refers to the density variance and is defined as

$$E_\rho = \frac{1}{2} \langle \rho^2 \rangle. \quad (2.12)$$

In HVDT, during the flow evolution,  $\bar{\rho}$  remains constant due to homogeneity, so that  $\rho_{,t}^* = \rho_{,t}$  and the rate of change of scalar energy per unit volume can be calculated by multiplying (2.1) by  $\rho$ . Using homogeneity, i.e.  $\langle (\ )_{,j} \rangle = 0$ , the transport equation turns into

$$\begin{aligned} \frac{1}{2} \langle \rho_{,t}^2 \rangle &= -\langle (\rho^* - \bar{\rho})(\rho^* u_j^*)_{,j} \rangle = -\langle [(\rho^* - \bar{\rho})\rho^* u_j^*]_{,j} \rangle + \frac{1}{2} \langle \rho_{,j}^{*2} u_j^* \rangle \\ &= \frac{1}{2} \langle (\rho^{*2} u_j^*)_{,j} \rangle - \frac{1}{2} \langle \rho^{*2} u_{j,j}^* \rangle \\ &= \frac{1}{2Re_0Sc_0} \langle \rho^{*2} (\ln \rho^*)_{,jj} \rangle \\ &= -\frac{1}{Re_0Sc_0} \langle \rho_{,j} \rho_{,j} \rangle. \end{aligned} \quad (2.13)$$

The resultant dissipation rate,  $\chi = (1/Re_0Sc_0) \langle \rho_{,j} \rho_{,j} \rangle$ , is similar to the dissipation rate for a passive scalar (Livescu, Jaberri & Madnia 2000; Daniel, Livescu & Ryu 2018).

#### 2.3.2. Total kinetic energy ( $E_{KE}$ )

The total kinetic energy is defined as

$$E_{KE} = \frac{1}{2} \langle \rho^* u_i^* u_i^* \rangle. \quad (2.14)$$

The rate of change of kinetic energy per unit volume is obtained by multiplying the momentum (2.2) by  $u_i^*$  ( $= u_i$ ) and averaging the resulting equation:

$$E_{KE,t} = \frac{g_i}{Fr^2} \langle \rho^* u_i \rangle + \langle \rho u_{j,j} \rangle - \langle u_{i,j} \tau_{ij}^* \rangle. \quad (2.15)$$

The first term on the right-hand side is the buoyancy-production term and is proportional to the mass flux defined by

$$a_i = \frac{\langle \rho u_i \rangle}{\bar{\rho}} = \tilde{U}_i - U_i = -\langle u_i'' \rangle. \quad (2.16)$$



The second (pressure-dilatation) term is the trace of the pressure-strain tensor and is the gain or loss of kinetic energy due to the work done by the change of specific volume during mixing. For the parameters considered here, this term is negligible compared to the other terms. However, since the flow is anisotropic, the components of the pressure-strain tensor (e.g.  $\langle pu_{1,1} \rangle$ ) are not negligible and they represent the primary mechanism of redistributing kinetic energy in different directions. The last term on the right-hand side is the total kinetic energy dissipation rate,  $\epsilon_{tot}$ .

2.3.3. Favre-averaged turbulent kinetic energy ( $E_{TKE}$ )

The Favre-averaged turbulent kinetic energy ( $E_{TKE}$ ) is defined as

$$E_{TKE} = \frac{1}{2} \langle \rho^* u_i'' u_i'' \rangle = \frac{1}{2} (\langle \rho^* u_i^* u_i^* \rangle - \bar{\rho} a_i a_i). \tag{2.17}$$

The terms on the right-hand side of (2.17) are the total kinetic energy ( $E_{KE}$ ) and mean kinetic energy ( $E_{MKE}$ ), respectively.

The transport equation for  $E_{TKE}$  can be written as (Livescu & Ristorcelli 2007)

$$E_{TKE,t} = a_i P_{,i} + \langle pu_{j,j}'' \rangle - \langle u_{i,j}'' \tau_{ij}^* \rangle. \tag{2.18}$$

The first term on the right-hand side is the turbulent kinetic energy production and the last term on the right-hand side is the turbulent kinetic energy dissipation rate ( $\epsilon$ ). Owing to homogeneity,  $\epsilon_{tot} = \epsilon = \langle u_{i,j}^* \tau_{ij}^* \rangle$ . Similarly,  $\langle pu_{j,j}'' \rangle = \langle pu_{j,j} \rangle$ .

2.3.4. Potential energy ( $E_{PE}$ )

The total available potential energy ( $E_{PE}$ ) for the triply periodic volume ( $V$ ) is calculated as

$$E_{PE}(t) = -\frac{g_i}{\mathcal{V}Fr^2} \int_{\mathcal{V}} (\rho^* - \bar{\rho}) x_i d\mathcal{V} - \int_{t=0}^{t \rightarrow \infty} \mathcal{F}_{E_p^*} dt, \tag{2.19}$$

where  $x_i$  is the relative height, which varies from 0 to  $2\pi$  in the direction opposite to the acceleration vector  $\mathbf{g}$ , and  $\mathcal{F}_{E_p^*} = -(g_i/\mathcal{V}Fr^2) \int_S u_j (\rho^* - \bar{\rho}) x_i dS_j$  is the flux of the potential energy through the boundaries. The change of the available potential energy can be derived as (Livescu & Ristorcelli 2007)

$$\begin{aligned} E_{PE,t} &= -\frac{\partial}{\partial t} \left( \frac{g_i}{\mathcal{V}Fr^2} \int_{\mathcal{V}} (\rho^* - \bar{\rho}) x_i d\mathcal{V} \right) - \mathcal{F}_{E_p^*} \\ &= -\frac{g_i}{Fr^2} \langle \rho^* u_i \rangle + \frac{g_i \bar{\rho}}{\mathcal{V}Fr^2} \int_S u_j x_i dS_j, \end{aligned} \tag{2.20}$$

where the first term is identical to the buoyancy-production term in (2.18), but with opposite sign, and the second term is a surface integral that goes to zero after averaging the results over different realizations.

2.4. Energy conversion rates in buoyancy-driven HVDT

In RTI under constant acceleration, the energy conversion ratio has been related to the growth rate of the RTI mixing-layer width in the alpha-group study (Dimonte *et al.* 2004). They reported an energy conversion rate from potential to kinetic energy ( $E_{KE}/\delta E_{PE}$ ) of  $0.46 \pm 0.04$  when 80% of the flow is molecularly mixed ( $\theta \approx 0.8$ ) within the mixing layer during the self-similar regime of RTI. However, this

asymptotic behaviour remains an open question, as Cabot & Cook (2006) found that, after a relatively flat stage,  $E_{KE}/\delta E_{PE}$  starts to increase again using a  $3072^3$  DNS with  $A = 0.5$ ; this change in behaviour corresponds to the end of the alpha-group simulations where the layer reaches the domain boundaries. In HVDT, since there is no self-similar stage during the growth regimes, we report the energy conversion rate separately for the two growth regimes (explosive and saturated growths) to explore  $A$  and  $Re_0$  effects on this ratio. Similar to RTI, we define  $\beta_{KE}$  as the ratio of the change in  $E_{KE}$  to the change in available  $E_{PE}$  as

$$\beta_{KE} = \frac{\Delta E_{KE}}{\Delta E_{PE}} = (E_{KE_{t_2}} - E_{KE_{t_1}}) \bigg/ \int_{t_1}^{t_2} E_{PE,t}(t) dt, \tag{2.21}$$

where  $\Delta E_{KE}$  is the change in  $E_{KE}$  and  $\Delta E_{PE}$  is the change in available  $E_{PE}$  between any two time instants chosen for analysis. We will also discuss this ratio for the turbulent kinetic energy ( $\beta_{TKE}$ ) and mean kinetic energy ( $\beta_{MKE}$ ). The  $\beta$  values are calculated by setting  $t_1$  and  $t_2$  in (2.21) to the normalized start and end times for the corresponding regime. For example, to calculate  $\beta_{TKE}$  for the explosive growth regime, the start time is set as  $t_1 = t/t_r = 0.1$ ; while the end time  $t_2$  is equal to the normalized time when the condition  $dE_{TKE}/dt > 0$  and  $d^2E_{TKE}/dt^2 = 0$  is reached.

2.5. *Transport equation for velocity–density joint mass density function (jMDF)*

Turbulent mixing as occurs in HVDT is a dynamic process where both local velocities and the fluid composition are coupled and integral to the mixing process. Here, in order to investigate the coupled effects of the composition (density) and velocity fluctuations on VD mixing, the transport equation of the density-weighted velocity–density joint p.d.f. (or velocity–density jMDF) is derived. As noted by Pope (1985) and Haworth (2010), for VD turbulence, the mass density function (MDF) is more useful compared to the p.d.f. because the resulting equations are simpler. In addition, the velocity–density jMDF is an effective way of exploring the coupled effects of composition and velocity fluctuations, which provides comprehensive information about the buoyancy-driven VDT evolution. The jMDF ( $\mathcal{F}$ ) is defined as

$$\mathcal{F}_{u_i\rho^*}(V_i, R; x_i, t) = R f_{u_i\rho^*}(V_i, R; x_i, t), \tag{2.22}$$

where  $f_{u_i\rho^*}(V_i, R; x_i, t)$  is the joint probability density function (j.p.d.f.) of the velocity and density fields.

Following Pope (1985), the j.p.d.f. can be calculated using the fine-grained p.d.f.,  $f^*$ , as  $f = \langle f^* \rangle = \langle \delta(u_i^* - V_i)\delta(\rho^* - R) \rangle$ , where  $\delta$  is the delta function, and  $V_i$  and  $R$  are the independent sample space variables. The details of the derivation can be found in appendix A; the final version can be written as

$$\begin{aligned} \frac{\partial \mathcal{F}}{\partial t} = & -\frac{\partial}{\partial V_i} \left[ \mathcal{F} \left\langle -\frac{P_i}{\rho^*} \bigg|_{V_i,R} - \frac{P_i}{\rho^*} \bigg|_{V_i,R} + \frac{\tau_{ij}^*}{\rho^*} \bigg|_{V_i,R} + \frac{1}{Fr^2} g_i \bigg|_{V_i,R} \right\rangle \right] \\ & - \frac{\partial}{\partial R} [\mathcal{F} \langle -\rho^* u_{j,j}^* |_{V_i,R} \rangle], \end{aligned} \tag{2.23}$$

where  $\langle Q |_{V_i,R} \rangle$  is the conditional expectation of the function  $Q(\rho^*, u_i^*; x_i, t)$  for specific velocity ( $u_i^* = V_i$ ) and density ( $\rho^* = R$ ) values. For the homogeneous case, the explicit spatial dependence drops from the averages. Thus, in homogeneous VDT,

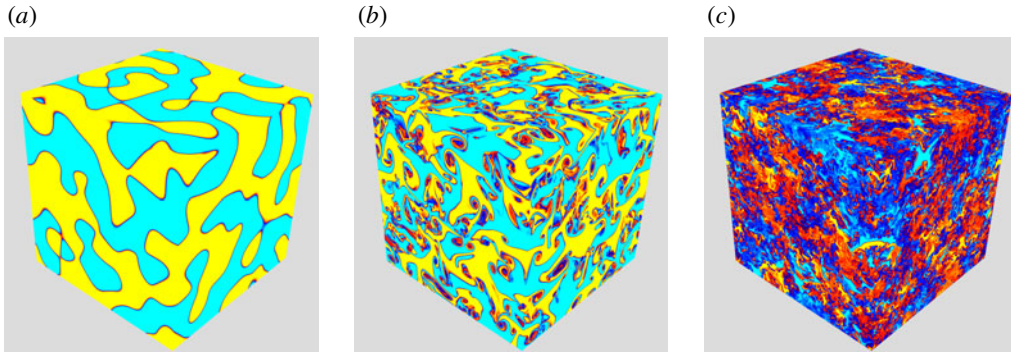


FIGURE 1. Three-dimensional visualization of the density field for A1Re0 case: (a) initially segregated patches of heavy and light fluids at  $t/t_r = 0$ ; (b) at intermediate times, mixing is induced by differential buoyancy forces ( $t/t_r \approx 2$ ); and (c) at late time ( $t/t_r \approx 3$ ), buoyancy forces decrease and this leads to decay of  $E_{TKE}$ .

equation (2.23) is four-dimensional. The first term on the right-hand side represents the transport of  $\mathcal{F}$  in the velocity sample space, while the second term represents the transport of  $\mathcal{F}$  in the density sample space (Pope 1985). The presence of the two terms indicates that any asymmetry of the density p.d.f. is carried over to the velocity p.d.f. (or *vice versa*). Both  $g_i$  and  $P_i$  are constant everywhere within the domain. However, since the pressure term is multiplied by the specific volume ( $1/\rho^*$ ), it leads to significant asymmetric behaviour at high  $A$ .

### 2.6. Conditional expectations

Owing to the large density variations among different fluid regions, differential inertial forces affect mixing (Livescu *et al.* 2010), as well as flow dynamics. Banerjee *et al.* (2010) utilized conditional expectations by using the density field as a fluid marker to study the dynamics of bubbles and spikes for their large- $A$  number RTI experiments. They found significant differences between the statistics calculated at the bubble side (defined as  $\rho < 0$ ) compared to the spike side (defined as  $\rho > 0$ ).

To further explore the structure of the HVDT flow, the conditional expectations of several quantities are discussed for each of the four flow regimes. These are related to the large (i.e. turbulent kinetic energy) as well as small (i.e. dissipation and enstrophy) scales. In particular, conditional dissipation highlighted in (2.23) is an important quantity in combustion models (Klimenko & Pope 2003). For binary VD flows in the incompressible limit, the mass fractions do not appear explicitly in the governing equations and can be completely determined from density. Therefore, the conditional expectations of  $E_{TKE}$ , dissipation of  $E_{TKE}$  and enstrophy ( $\omega^2$ ) are evaluated with respect to the local density (i.e.  $\langle \rho^* u_i' u_i'' |_{\rho^*=R} \rangle$ ).

### 3. Flow evolution

In HVDT, two fluids with different densities are initially segregated into random regions in a triply periodic domain and are subjected to an acceleration  $g_1$  (figure 1a). At early times, turbulence is generated as the two fluids start moving in opposite directions due to differential buoyancy forces (figure 1b). Meanwhile, mixing is initiated by molecular diffusion and enhanced by stirring induced by buoyancy-generated motions. As the fluids become molecularly mixed, the buoyancy forces

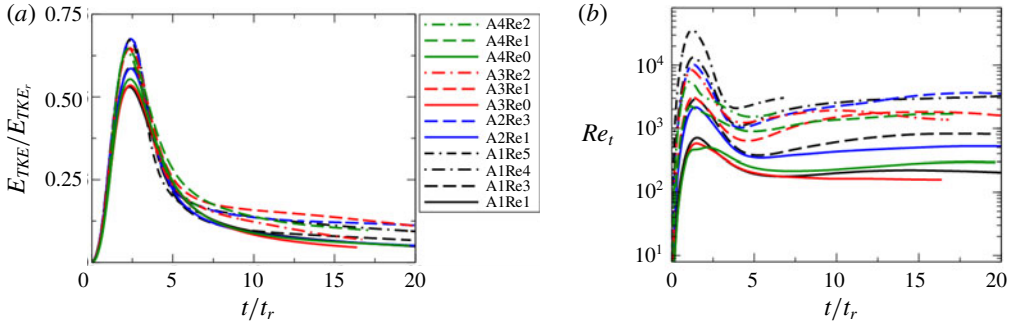


FIGURE 2. Evolutions of (a) the normalized Favre turbulent kinetic energy ( $E_{TKE}/E_{TKE,r}$ ) and (b) the turbulent Reynolds number ( $Re_t$ ).

decrease and, at some point,  $E_{TKE}$  dissipation overcomes  $E_{TKE}$  production. This leads to a decay of  $E_{TKE}$  (see figure 1c).

The time evolutions of  $E_{TKE}/E_{TKE,r}$  ( $\langle \rho^* u_i'' u_i'' \rangle / \bar{\rho} U_r^2$ ) and turbulent Reynolds number ( $Re_t$ ) are shown in figure 2. The values are plotted as a function of time ( $t/t_r$ ). As seen in figure 2(a), the maximum of  $E_{TKE}/E_{TKE,r}$  asymptotes to a finite value as  $Re_{b0}$  increases; this observation is consistent with the prediction by Batchelor *et al.* (1992) at very large  $Re_{b0}$  values for the Boussinesq limit. In addition, Batchelor *et al.* (1992) also predicted that the  $E_{TKE}$  maxima occur at the same normalized time instant, if  $Re_{b0} > 256$ . For our VD cases at  $Re_{b0} > 512$ , all  $E_{TKE}$  maxima occur at approximately  $t/t_r \approx 2.3$ , as seen in figure 2(a) (this observation was also hinted at by Livescu & Ristorcelli (2007) using low- $Re$  data); this further justifies the scaling used here.

Figure 2(b) presents the evolution of  $Re_t$ ; it is observed that an increase in  $Re_0$  leads to significant increase in  $Re_t$ . For the simulations reported in this paper, the largest  $Re_t$  value is  $\sim 36\,000$ , corresponding to a Taylor Reynolds number ( $Re_\lambda$ ) of 490, for the lowest  $A$  ( $= 0.05$ ) number case with  $2048^3$  resolution (A1Re5 case). In addition, for the largest  $A$  ( $= 0.75$ ) number case with the  $2048^3$  resolution (A4Re2 case),  $Re_t$  reaches a maximum value of 5500, with  $Re_\lambda = 191$ . The variation of  $Re_t$  with  $A$ , at the same  $Re_0$ , is non-monotonic. Thus, the largest  $Re_t$  values are obtained for  $A = 0.5$ . This behaviour is due to the opposing influences of buoyancy-induced stirring (which increases at early times with  $A$ ) and molecular mixing (which is enhanced by stirring), and is explained in more detail below. At late times,  $Re_t$  is non-decreasing, as suggested by Batchelor *et al.* (1992), even though the effective Atwood number asymptotes to zero. Thus, buoyancy-mediated turbulence decay is fundamentally different from regular turbulence decay.

Figure 3 presents the ratio of the time scales for turbulent kinetic energy and density variance equations, which is defined as

$$\gamma = \frac{E_{TKE}}{\epsilon} \bigg/ \frac{E_\rho}{\chi} = \frac{E_{TKE} \chi}{E_\rho \epsilon}. \quad (3.1)$$

In low-order turbulent mixing models,  $\gamma$  is assumed to be a constant and the scalar dissipation  $\chi$  is estimated using the turbulent kinetic energy dissipation  $\epsilon$  (Livescu *et al.* 2000; Kolla *et al.* 2009; Daniel *et al.* 2018). For passive scalar mixing with mean scalar gradient forcing  $\gamma \approx 2$  (Overholt & Pope 1996; Kolla *et al.* 2009), other forcing mechanisms or flow conditions can lead to different values (Daniel *et al.* 2018). For reacting flows, much larger values can be obtained (Livescu *et al.* 2000).

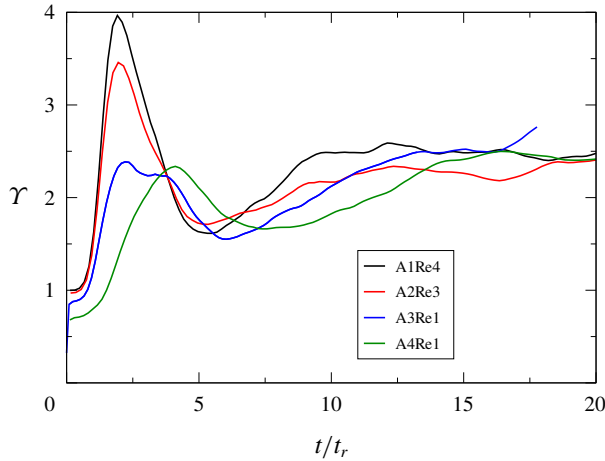


FIGURE 3. Evolution of the ratio of the time scales for turbulent kinetic energy and density variance equations ( $\gamma$ ) for different  $A$  numbers.

In HVDT,  $\gamma$  is a dynamic parameter during the earlier evolution of the flow, and the dissipation of the density field and  $E_{TKE}$  must be captured separately until the gradual decay regime where buoyancy forces weaken.

As observed in figures 1 and 2, HVDT includes the birth, growth and decay of buoyancy-driven turbulence; the turbulence generation and decay stages contain unique physics that can be related to a wide range of flows discussed previously. Based on the flow behaviour, we have subdivided the flow evolution into four distinct regimes: (I) explosive growth, (II) saturated growth, (III) fast decay and (IV) gradual decay. This classification allows us to study the connection between this idealized flow and RTI, RMI as well as other flows that contain VD dynamics.

To illustrate these regimes, figure 4 shows the time evolution of  $E_{TKE}/E_{TKE}$ , its time derivative,  $E_{KE}/E_{KE}$  ( $\langle \rho^* u_i^* u_i^* \rangle / \bar{\rho} U_r^2$ ) and  $E_{MKE}/E_{MKE}$  ( $a_i a_i / U_r^2$ ) for different  $A$  numbers. The  $E_{MKE}$  values are higher and lead to a phase difference between the  $E_{TKE}$  and  $E_{KE}$  evolutions for larger  $A$  numbers, where the inertial differences between the light- and heavy-fluid regions are important; such differences are negligible at low  $A$  numbers. The amounts of pure light and heavy fluids are also plotted in figure 4. The 5% and 95% density cutoffs are used to define the pure light and heavy fluids. The pure light fluid is considered as having a density below  $\rho_{pl}$ , where  $\rho_{pl} = \rho_1 + 0.05(\rho_2 - \rho_1)$ , and the pure heavy fluid is defined as having a density above  $\rho_{ph}$ , where  $\rho_{ph} = \rho_1 + 0.95(\rho_2 - \rho_1)$ .

At  $t/t_r = 0$  molecular diffusion is important, since the flow starts from rest. However, as the fluids are accelerated, i.e.  $g_1$  increases from 0 to 1 in  $t/t_r = 0.1$ , turbulence diffusion starts dominating molecular diffusion. Turbulence birth is followed by intense turbulence generation, which is divided into two subregimes: (I) explosive growth, where  $E_{TKE}$  growth accelerates, as  $d^2 E_{TKE}/dt^2 > 0$ ; and (II) saturated growth, where the rate of increase of turbulence fluctuations starts decreasing,  $d^2 E_{TKE}/dt^2 < 0$ . Regime (I) ends at  $t/t_r \approx 1.1$ , when  $dE_{TKE}/dt$  reaches its maximum, while regime (II) ends at  $t/t_r \approx 2.3$ , when  $dE_{TKE}/dt = 0$ . The amount of pure heavy fluids remains significant during these two regimes; however, at high Atwood numbers there is also a significant asymmetry between pure light- and heavy-fluid volumes, which starts to develop during saturated growth. Eventually, the cumulative effect of

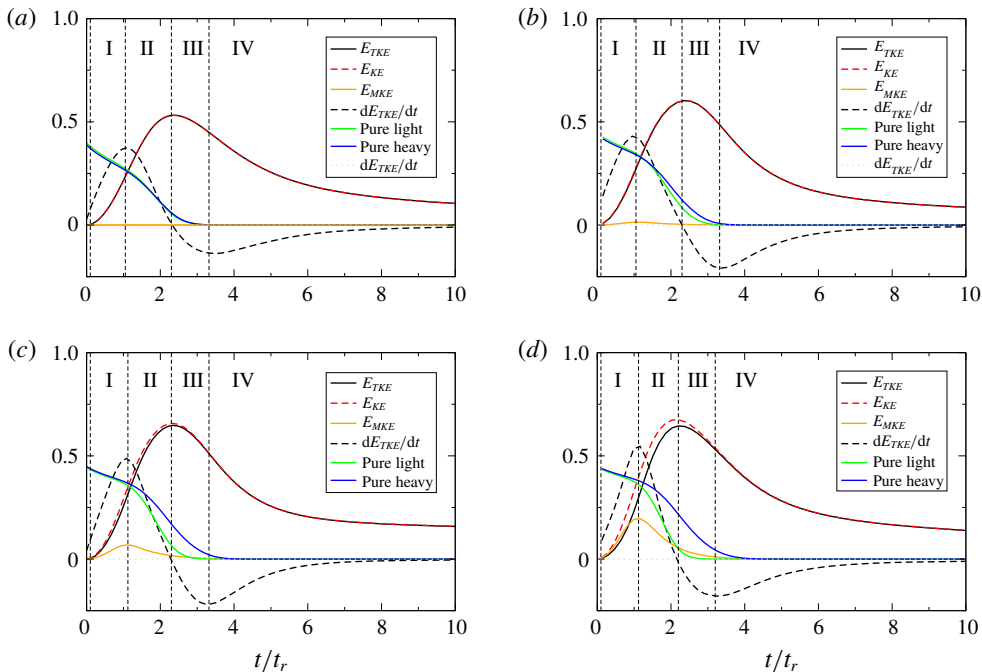


FIGURE 4. Evolution of the normalized  $E_{TKE}$ , its time derivative,  $E_{KE}$ ,  $E_{MKE}$  and the volume fractions of the pure light and heavy fluids for the cases (a) A1Re1, (b) A2Re1, (c) A3Re1 and (d) A4Re1.

molecular diffusion becomes large enough that, once again, it dominates the turbulence production and turbulence starts decaying. Flow characteristics also change during turbulence decay, so that this part of flow evolution is broken up into two subregimes: (III) fast decay, where  $d^2E_{TKE}/dt^2 < 0$ ; and (IV) gradual decay, where  $d^2E_{TKE}/dt^2 > 0$  and the decay process becomes slow and lengthy. Regime (III) lasts until  $t/t_r \approx 3.2$ , when  $dE_{TKE}/dt$  reaches its minimum. Regime (IV) is the only part of flow evolution that becomes self-similar. During fast decay, there is still a sizeable amount of pure heavy fluid, while the pure light fluid vanishes from the flow. Eventually, the pure heavy fluid also vanishes, as the gradual decay regime starts.

Atwood number has a limited effect on the normalized time instants where the regimes start, even though the flow structure dramatically differs by increasing the density ratio between the two fluids. The  $Re_0$  value also does not have any significant effect on these normalized time instants, and is not shown here for brevity. All regimes have their own characteristics concerning molecular mixing, energy conversion rates and dependence on  $A$  and  $Re_0$  numbers. The flow physics are discussed in detail in the next section for each of the four regimes.

While the initial conditions are random, the flow is not turbulent from the start. This raises an important question: When does the turbulence become fully developed? This question is also related to the concept of mixing transition (Dimotakis 2000). Above the mixing transition, the flow characteristics become independent of  $Re_t$ . Here, the Reynolds number increases during the early stages of the flow evolution and reaches larger values for cases with smaller viscosity (see figure 2b). For each Atwood number, we investigate separately the convergence of turbulence statistics as the Reynolds number increases. Owing to the highly dynamic nature of the

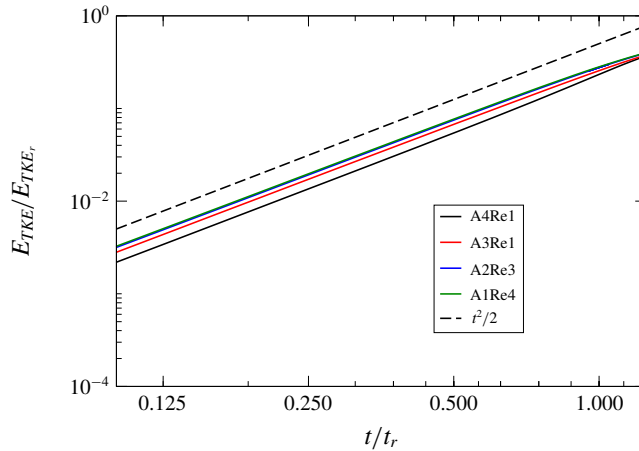


FIGURE 5. Growth of  $E_{TKE}$  during explosive growth.

flow and highly asymmetric evolution for the high- $A$ -number cases, we use direct comparisons between the cases with lower and larger  $Re_t$  values (especially comparing  $1024^3$  simulations versus  $2048^3$  simulations) to determine whether any flow quantity becomes insensitive to increase in  $Re_t$  in different flow regions. As a result, we show (in the next section) that different turbulent quantities reach their asymptotic behaviour at different time instants, which also depends on the Atwood number. Moreover, for the higher- $A$ -number cases, this occurs at different times for different density regions.

## 4. Flow regimes

### 4.1. Explosive growth

Explosive growth is initiated when the large structures in the domain start to move fast enough to generate turbulence. As the generation of  $E_{TKE}$  is accelerated in this regime ( $d^2E_{TKE}/dt^2 > 0$ ), there are certain similarities with the core region of the RTI mixing layer. In RTI, when the flow becomes self-similar,  $h$  (the mixing-layer width) grows quadratically, with the leading-order term of the form  $Ag t^2$ . Consequently, the turbulent kinetic energy variation, which can be estimated as  $\approx 1/2\dot{h}^2$ , also grows quadratically. Figure 5 shows that the growth of  $E_{TKE}$  during explosive growth scales as  $\approx t^2$ , similar to RTI.

During this regime, the amounts of pure fluids start decreasing slowly as mixing is initiated (figure 4). This decay is slow, as molecular mixing occurs mostly at the interface of the pure fluids, where stirring first develops. No significant differences between the behaviour of the pure light and heavy fluids are observed for the  $A$  numbers investigated in this paper.

Figure 6 shows the three-dimensional (3-D) evolution of the mole fraction (figure 6a) and the velocity magnitude (figure 6b) for  $A = 0.05$  and  $A = 0.75$  (low- and high-density ratios) at different time instants. At  $t/t_r = 0$ , the domain consists of pure light- and heavy-fluid patches separated from each other by thin layers; the mole fraction distribution is identical for both cases. At  $t/t_r = 0.65$ , when the flow experiences a period of explosive growth, the behaviour of the density field (or mole fraction) is still similar for both low and high  $A$  numbers. The large structures are observed to conserve their shapes during this regime and do not attend to molecular mixing; this is consistent with the slow decrease of the volume fractions of pure

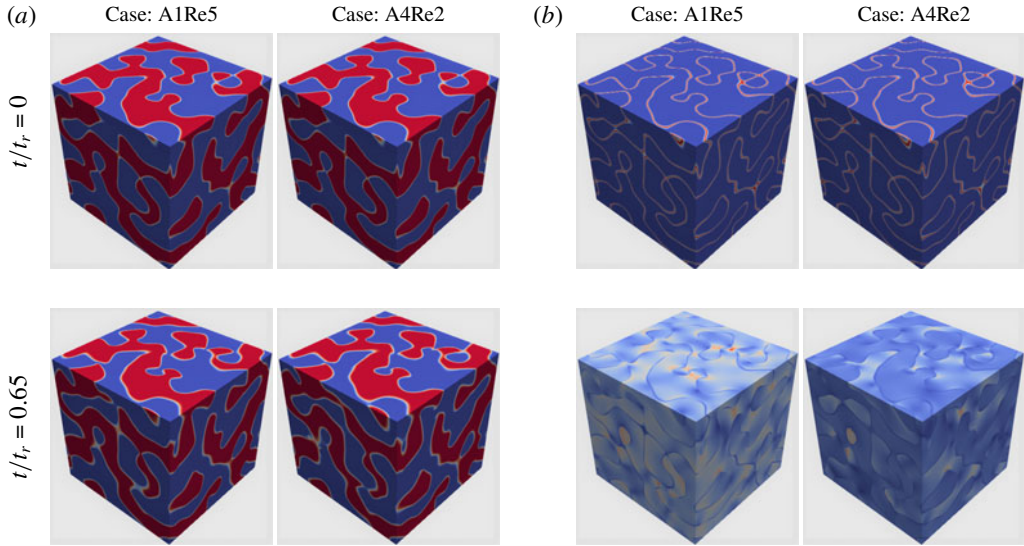


FIGURE 6. Three-dimensional visualizations of (a) the mole fraction, where blue represents the pure light fluid ( $\chi_h = 0$ ,  $\chi_l = 1$ ) and red represents the pure heavy fluid ( $\chi_h = 1$ ,  $\chi_l = 0$ ), and (b) the velocity magnitude ( $\sqrt{u_1^2 + u_2^2 + u_3^2}$ ), where blue represents the minimum velocity magnitude and red represents the maximum velocity magnitude, for the cases  $A = 0.05$  (A1Re5) and  $A = 0.75$  (A4Re2). The top row shows 3-D contours at  $t/t_r = 0$  while bottom row displays contours at  $t/t_r = 0.65$ .

fluids in figure 4. However, at  $t/t_r = 0.65$ , the velocity field is very different for low and high  $A$  numbers. At first glance, the velocity field is more homogeneously distributed for the low- $A$ -number case; whereas for the high- $A$ -number case, the largest velocity magnitudes are more concentrated within regions that are occupied by the lighter-than-average fluid.

#### 4.1.1. Energy conversion rates

Using (2.21), the energy conversion rates are calculated for different  $A$  and  $Re_0$  numbers. Figures 7 and 8 show the variations of  $\beta_{KE}$ ,  $\beta_{TKE}$  and  $\beta_{MKE}$  with  $A$  and  $Re_0$  numbers. During explosive growth, high levels of turbulence generation occur, as most of the potential energy lost gets converted to kinetic energy ( $\beta_{KE} > 90\%$ ). For cases with the same  $Re_0$ ,  $\beta_{KE}$  is similar for all  $A$  numbers; however, it increases slightly with an increase in the value of  $Re_0$ . Meanwhile,  $\beta_{TKE}$  is found to dramatically decrease upon increase of the  $A$  number. As also observed in figure 4, for moderate (0.5) and high (0.75)  $A$  numbers, there is a delay in  $E_{TKE}$  growth compared to  $E_{KE}$ . This delay might be attributed to the larger inertial differences between heavy- and light-fluid regions. Initially, heavy-fluid regions may not be stirred as efficiently as the light-fluid regions due to their larger inertia and this causes a decrease in  $\beta_{(TKE)}$  for larger  $A$  numbers. In addition, the difference between  $E_{KE}$  and  $E_{TKE}$  is stored within  $E_{MKE}$ , which acts as a reservoir for  $E_{TKE}$  for the subsequent regimes in the flow evolution. Furthermore, for the low- $A$ -number case, the energy conversion rates tend to asymptote to constant values, while for the high- $A$ -number case, they asymptote to constant values when  $Re_0$  is increased (see figure 8). This indicates that the flow undergoes the mixing transition in terms of energy conversion rates as the effects of the increase in the  $R_0$  become negligible.



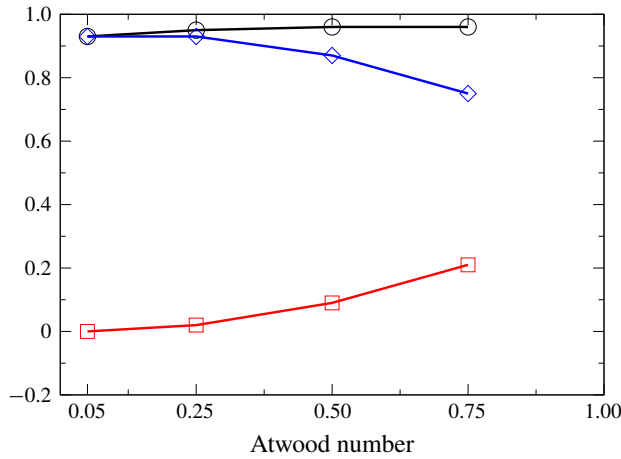


FIGURE 7. Atwood-number effects on energy conversion rates  $\beta_{KE}$  (black line),  $\beta_{TKE}$  (blue line) and  $\beta_{MKE}$  (red line) during explosive growth.

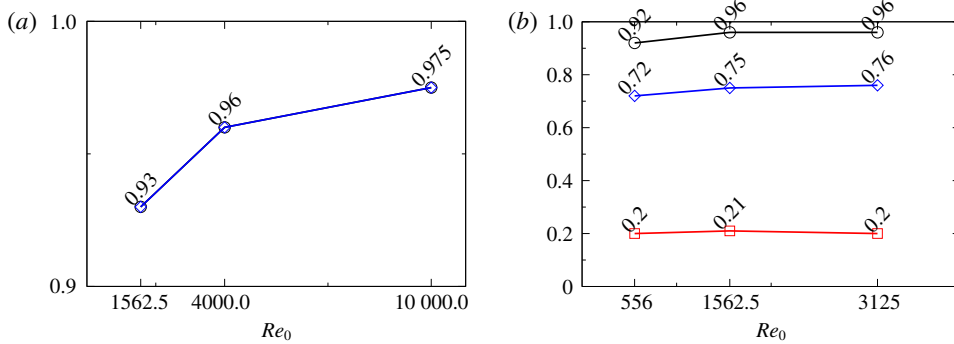


FIGURE 8. Reynolds-number effects on energy conversion rates  $\beta_{KE}$  (black line),  $\beta_{TKE}$  (blue line) and  $\beta_{MKE}$  (red line) during explosive growth regime for (a)  $A = 0.05$  (blue and black lines are identical, while the red line is close to zero) and (b)  $A = 0.75$ .

#### 4.1.2. Atwood-number effects on p.d.f. evolutions

##### Density p.d.f.

Figure 9 presents  $A$ - and  $Re_0$ -number effects on the density p.d.f. during explosive growth ( $t/t_r = 0.65$ ). In both panels, the density field is represented by the heavy fluid's mole fraction ( $\chi_h$ ); due to incompressibility,  $\chi_h = (\rho^* - \rho_1)/(\rho_2 - \rho_1)$ . The p.d.f. behaves similarly for low and high  $A$  numbers. In addition, the  $Re_0$  number does not have any significant effect on these p.d.f.s. The  $A1Re1$  case is slightly more mixed compared to the other cases due to its higher initial mixing state as described in § 2.2. Weak  $A$ -number dependence on density p.d.f. is consistent with the observations reported for figure 6. The mixing rates are smaller during this regime and stirring is mostly localized; as a result  $A$ -number effects on density p.d.f. are not prominent.

##### Velocity–density jMDF

As observed in figure 6, the velocity field starts to behave differently for low and high  $A$  numbers right after the acceleration ramp-up; this is noticeably earlier than

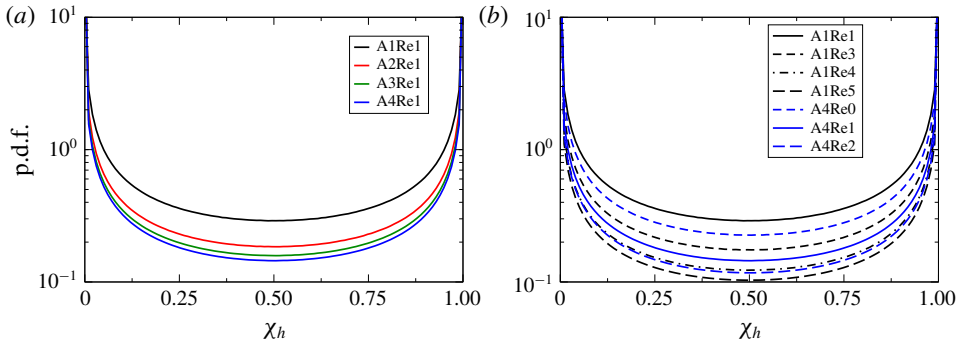


FIGURE 9. The p.d.f. of density field for the different (a)  $A$  and (b)  $Re_0$  values at  $t/t_r = 0.65$ .

the density field. The flow is highly anisotropic in the vertical (accelerated) direction (Livescu & Ristorcelli 2008). Figure 10 shows the normalized jMDF ( $\log(\mathcal{F}/\bar{\rho})$ ) corresponding to the vertical component of the velocity field ( $u_1/u_r$ ) for the low- and high- $A$ -number cases (at  $t/t_r = 0.65$ ). It is observed that, for both low and high  $A$  numbers, lighter-fluid regions mostly move in the opposite direction of the acceleration field, while heavier-fluid regions mostly move in the acceleration field direction. During explosive growth, the jMDF has a double-delta shape with two peak points, as a result of initial double-delta density p.d.f.; the peak points are on the negative and positive velocity sides. These two peaks indicate that there are two different velocity subdistributions within the flow. Similar to RTI, the negative side represents the velocity distribution within pure heavy-fluid regions (which are mostly going down) and the positive side represents the velocity distribution within pure light-fluid regions (which are mostly going up). This is also consistent with high- $A$ -number experiments (Banerjee *et al.* 2010), where it is reported that lighter-fluid regions mostly move in the opposite direction of the acceleration field as they are associated with the rising bubbles, and heavier-fluid regions mostly move in the same direction of the acceleration field as they are associated with the dropping spikes. Moreover, for low- $A$ -number cases, the velocity distribution is almost symmetric within the different regions of the flow (for the different levels of  $\chi_h$ ) and density and velocity fields are moderately correlated. However, for high- $A$ -number cases, the velocity distribution within the different regions of the flow becomes highly asymmetric and the pure light-fluid regions move much faster than the pure heavy-fluid regions. Those faster motions for larger  $A$  numbers can be attributed to the  $P_{,i}/\rho^*$  term in (2.23), which is asymmetric due to the specific volume variation. In the light fluid,  $P_{,i}/\rho^*$  becomes large and, since turbulence is not developed yet, the nonlinear terms do not compensate for this variation.

#### 4.1.3. Conditional expectations

In this subsection, we present the conditional expectations of  $E_{TKE}$ ,  $E_{TKE}$ , dissipation and enstrophy to study  $A$  and  $Re_0$  effects on the asymmetry with respect to the density field.

##### Conditional expectation of $E_{TKE}$

The effects of variation of  $A$  and  $Re_0$  numbers on conditional expectations of  $E_{TKE}$  are shown in figure 11. For higher  $A$  numbers, light-fluid regions become more stirred

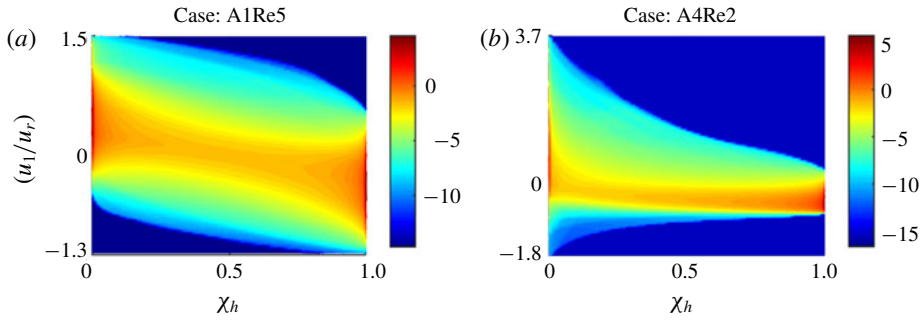


FIGURE 10. Normalized jMDFs ( $\log(\mathcal{F}/\bar{\rho})$ ) for (a)  $A = 0.05$  (A1Re5) and (b)  $A = 0.75$  (A4Re2) cases displayed at  $t/t_r = 0.65$ .

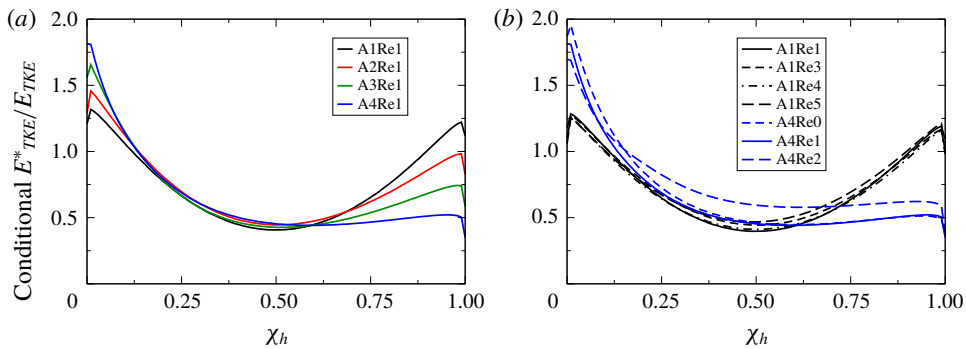


FIGURE 11. Atwood- and Reynolds-numbers effects on conditional expectation of  $E_{TKE}$  during explosive growth regime ( $t/t_r = 0.65$ ).

compared to heavy-fluid regions. This is also illustrated in the asymmetric shape of the jMDF (see figure 10). Thus,  $\langle \rho^* u''_i u''_i |_{\rho^*=R} \rangle$  within the lightest regions ( $\sim \rho_1$ ) is larger than  $E_{TKE}$  for the high  $A = 0.75$  case. The  $Re_0$  value has a relatively small effect on the distribution of the  $E_{TKE}$  within the different regions of the flow during explosive growth. In addition, the  $E_{TKE}$  values are larger in the lighter-fluid regions compared to the heavier-fluid regions, irrespective of the Reynolds number. This effect is the largest for the  $A = 0.75$  cases. The larger  $E_{TKE}$  values may also lead to earlier mixing transition in those regions. This is discussed in detail below.

*Conditional expectation of  $E_{TKE}$  dissipation*

The conditional expectation of the dissipation of  $E_{TKE}$  is plotted in figure 12. For the lowest- $A$ -number case, dissipation takes its highest values around the mean density. However, for the larger- $A$ -number cases, the peak of dissipation moves to lighter-fluid regions. This observation is consistent with figure 10, where we observed the velocity distribution to be much wider in the lighter-fluid region, thereby causing larger velocity gradients within the region.

Increasing  $A$  and/or  $Re_0$  increases the local values more than statistics based on the whole volume. When local values become much larger than the average value, these are usually called ‘extreme events’ within the flow. For the same  $Re_0$  values, the maximum local average (of dissipation) is larger compared to cases with lower  $A$  numbers (see figure 12a). Moreover, for the A1Re5 case,  $E_{TKE}$  dissipation within the

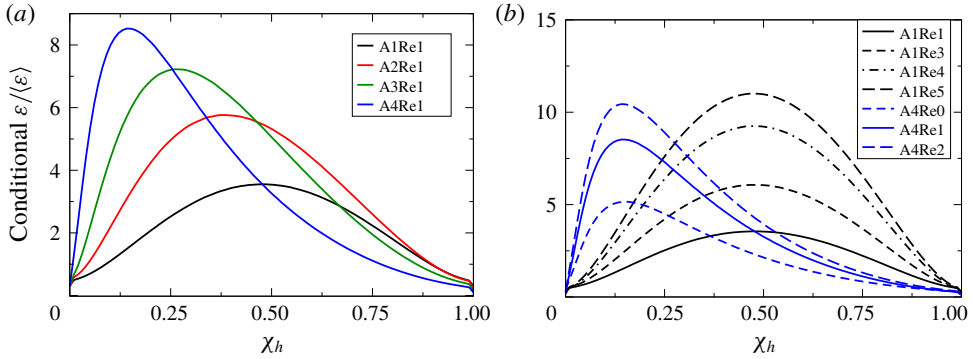


FIGURE 12. Atwood- and Reynolds-numbers effects on conditional expectation of  $E_{TKE}$  dissipation during explosive growth regime ( $t/t_r = 0.65$ ).

fully mixed regions is more than 10 times larger than its volume average; while for the A1Re1 case,  $E_{TKE}$  dissipation within the fully mixed regions is only three times larger than its volume average (see figure 12b). These larger local values indicate that both increasing  $A$  and/or  $Re_0$  numbers may increase the probability of occurrence of ‘extreme events’ within the flow.

#### Conditional expectation of enstrophy

The conditional expectations of the components of the enstrophy ( $\omega^2$ ) in vertical and horizontal directions and the total enstrophy are plotted in figures 13(a) and 13(b), respectively. During this regime, the enstrophy behaves very similarly to dissipation, and becomes asymmetric at larger  $A$  numbers. In addition, consistent with observations reported for dissipation, the local enstrophy values become larger than the volume average values upon increasing both  $Re_0$  and  $A$  numbers. Both dissipation and enstrophy are considered indicative of small-scale behaviour (Pope 2000); thus, the asymmetric behaviour of these quantities indicates asymmetry even at small-scale motions at large  $A$  numbers ( $A \geq 0.5$ ). It is also observed (see figure 13a) that the vertical component of the enstrophy is much smaller than horizontal components; for example, for the A1Re1 and A4Re1 cases,  $\omega_h^2$  are 10 and five times larger than  $\omega_v^2$ , respectively. This implies that the flow is anisotropic even at small scales. This aspect is discussed in the spectral evolution section (§ 5).

#### 4.2. Saturated growth

The time instant when  $E_{TKE}$  growth starts to slow down (such that  $d^2E_{TKE}/dt^2 < 0$ ) is chosen as the onset of the saturated growth regime. The 3-D evolution of the heavy-fluid mole fraction and the velocity during saturated growth are plotted in figure 14 for the low ( $A = 0.05$ ) and high ( $A = 0.75$ )  $A$  numbers. Both density and velocity fields start to behave differently for different  $A$  numbers. During this period, the stirring within the flow is no longer localized and large scales start to participate in the stirring process. The turbulent intensities become large and density gradients are increased, indicating higher mixing rates within the flow. As shown in figure 4, the amounts of pure light and heavy fluids continue to decrease, but at a rate faster than during explosive growth. In addition,  $A$ -number effects become prominent; for larger  $A$  numbers, the amounts of pure light and heavy fluids dramatically deviate from each other, indicating different mixing rates within the different flow regions,

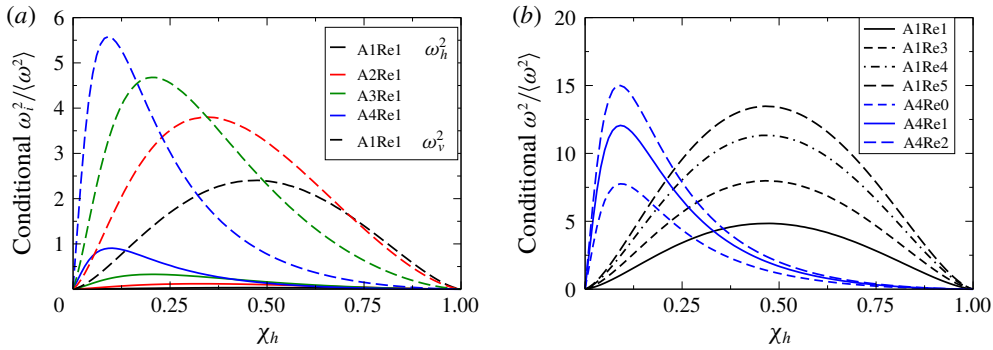


FIGURE 13. Atwood- and Reynolds-numbers effects on conditional expectation of (a) vertical ( $\omega_v^2 = \omega_1^2$ ) and horizontal ( $\omega_h^2 = (\omega_2^2 + \omega_3^2)/2$ ) enstrophy components and (b) total enstrophy during regime (I) explosive growth ( $t/t_r = 0.65$ ).

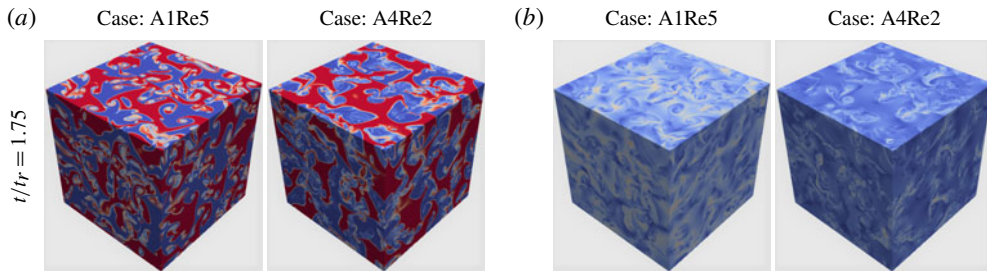


FIGURE 14. Three-dimensional visualization of (a) the mole fraction and (b) the velocity magnitude ( $\sqrt{u_1^2 + u_2^2 + u_3^2}$ ) for the cases  $A = 0.05$  (A1Re5) and  $A = 0.75$  (A4Re2) are displayed at  $t/t_r = 1.75$ .

similar to results observed by Livescu & Ristorcelli (2008). This breaks the symmetry of the density p.d.f., which adds more complexity to the problem. Below, it is shown that, for high  $A$  numbers, the asymptotic behaviour with respect to the Reynolds number occurs earlier within pure light-fluid regions than pure heavy-fluid regions, which is taken to signify faster mixing transition within the light-fluid regions.

#### 4.2.1. Energy conversion rates

During saturated growth, interestingly, for the same  $Re_0$  values, the relationship between the energy conversion rates and  $A$  number is not monotonic (see figure 15). Both  $\beta_{KE}$  and  $\beta_{TKE}$  peak at around  $A$ -number values of 0.25–0.5. The energy conversion rates are highest at moderate  $A$  numbers. In addition,  $\beta_{TKE}$  is greater than  $\beta_{KE}$  (see figure 4a). The stored energy in  $E_{MKE}$  is released to feed into  $E_{TKE}$ , which leads to  $\beta_{KE} < \beta_{TKE}$  and  $\beta_{MKE} < 0$ . Note that  $E_{MKE}$  is decreasing during saturated growth, which is also consistent with  $\beta_{MKE} < 0$  (see figure 4). It is also found that both low- and high- $A$  energy conversion rates tend to converge by increasing  $Re_0$ , indicating that the flow is beyond the mixing transition during the saturated growth regime in terms of the energy conversion rates (see figure 16).

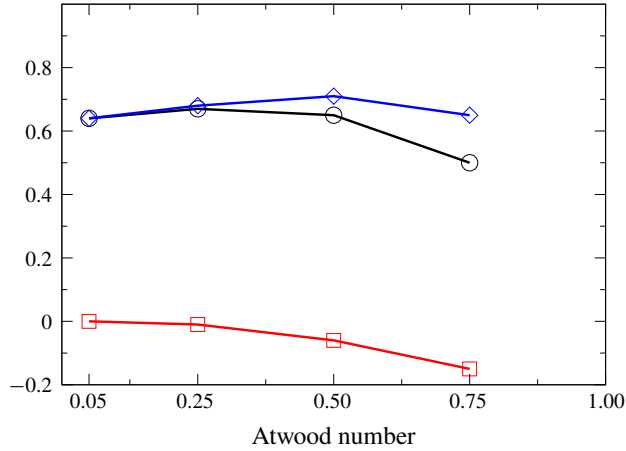


FIGURE 15. Atwood-number effects on energy conversion rates  $\beta_{KE}$  (black line),  $\beta_{TKE}$  (blue line) and  $\beta_{MKE}$  (red line) during saturated growth regime.

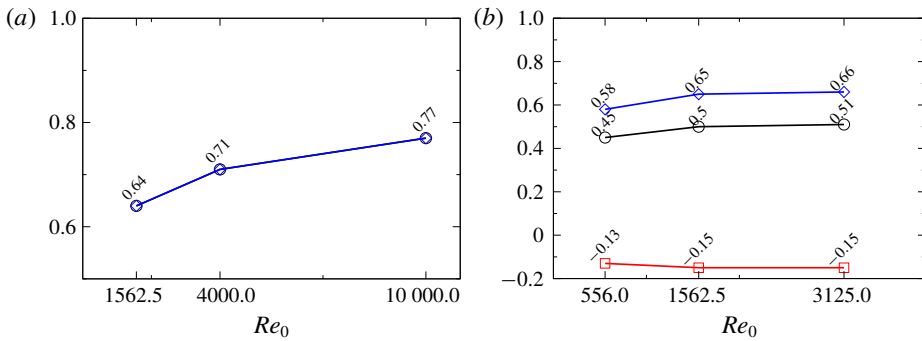


FIGURE 16. Reynolds-number effects on energy conversion rates  $\beta_{KE}$  (black line),  $\beta_{TKE}$  (blue line) and  $\beta_{MKE}$  (red line) during saturated growth regime for (a)  $A=0.05$  (blue and black lines overlap and red line is close to zero) and (b)  $A=0.75$ .

4.2.2. Atwood-number effects on p.d.f. evolutions

Density p.d.f.

Livescu & Ristorcelli (2008) found that increasing the  $A$  number breaks the symmetry of the mixing rates and leads to asymmetric density p.d.f.s. In their study, the reported results are for  $A$  number equal to 0.5, with maximum domain size of  $512^3$ , which was around the mixing transition threshold. The current work builds on that study to further investigate the asymmetric behaviour of the density p.d.f. evolution; density p.d.f.s for both larger  $A$  number ( $A=0.75$ ) and larger domain sizes up to  $2048^3$  (leading to much larger  $Re_i$  values) are presented. Figure 17 presents density p.d.f.s; the shape of the p.d.f. is distinctly different for different  $A$  numbers. For the large  $A$  number, the lightest-fluid regions mix faster than the heaviest-fluid regions. The density p.d.f. exhibits peak values at lighter-than-average fluid regions; this peak shifts to even lighter-fluid regions upon increasing the  $A$  number.

As discussed in §3, in order to determine whether a certain quantity is fully developed (i.e. beyond the mixing transition), we check if the time evolution of the

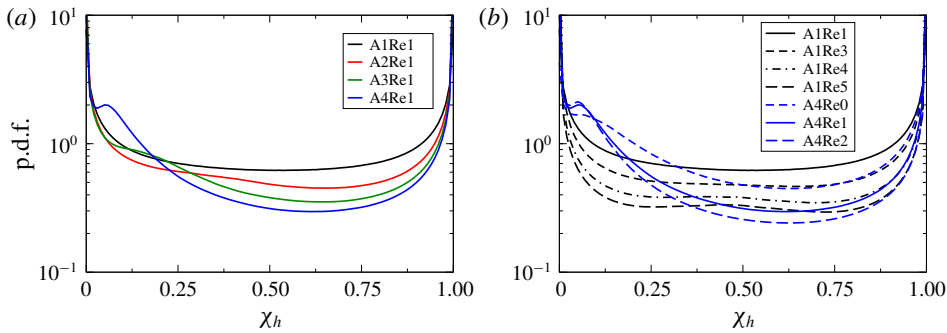


FIGURE 17. The p.d.f. of density field for the different (a)  $A$  and (b)  $Re_0$  values at  $t/t_r = 1.75$ .

quantity in question becomes independent of  $Re_t$ . The authors are of the opinion that for HVDT there is no single threshold that could determine whether the flow is beyond the mixing transition and that different quantities reach this transition differently. In figure 17(b), for the lowest- $A$ -number case of  $A = 0.05$ ,  $Re_0$  has minimal effect on the p.d.f. However, for large- $A$ -number cases, it is observed that only the lighter-fluid regions tend to become insensitive to an increase in  $Re_0$ . The variation of the density p.d.f. in the heavier-fluid regions is still large for the high  $A = 0.75$  cases (the cases A075Re3 and A075Re2), even if we compare the cases with the largest two  $Re_0$  values. This indicates that mixing transition may occur at earlier times for the lighter-fluid regions than the heavier-fluid regions when considering the density p.d.f. This is also consistent with the conditional expectation of  $E_{TKE}$  (see figure 11), which was observed to be much larger in lighter-fluid regions compared to heavier-fluid regions.

#### Velocity–density jMDF

The jMDF behaviour for low- and high- $A$ -number cases during the saturated growth regime is shown in figure 18. For the low- $A$ -number case, the jMDF is relatively symmetric with respect to the mole fraction at small velocity magnitudes. There is a slight asymmetry near the largest velocity magnitudes; the jMDF peaks at the light-fluid side at large positive velocities and on the heavy-fluid side at large negative velocities. In addition, at each heavy-fluid mole fraction level, the jMDF remains quasi-Gaussian, with the peak moving slightly from positive to negative velocities as  $\chi_h$  varies from 0 to 1. The jMDF is more complex for the high- $A$ -number case. Thus, the jMDF shape is wider at small values of  $\chi_h$ . At all  $\chi_h$ , the jMDF is asymmetric and skewed towards positive velocity values, though the asymmetry decreases compared to the explosive growth regime. A longer tail for positive values of the vertical velocity indicates more extreme upward motions in the flow, similar to that observed in the explosive growth.

#### 4.2.3. Conditional expectations

##### Conditional expectation of $E_{TKE}$

The  $A$ - and  $Re_0$ -number effects on the conditional expectation of  $E_{TKE}$  are shown in figure 19. At low  $A$ ,  $E_{TKE}$  is mostly balanced between lighter and heavier regions of the flow. As  $A$  increases at fixed  $Re_0$  value, the conditional expectation becomes asymmetric, with larger values in low- to moderate-density regions (figure 19a).

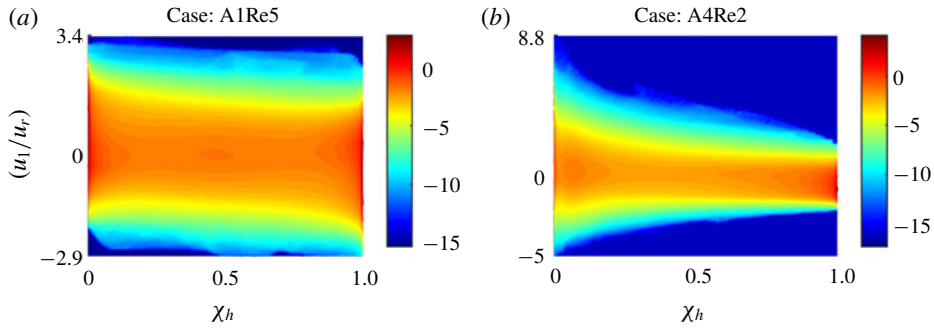


FIGURE 18. Normalized jMDFs ( $\log(\mathcal{F}/\bar{\rho})$ ) for (a)  $A = 0.05$  (A1Re5) and (b)  $A = 0.75$  (A4Re2) cases displayed at  $t/t_r = 1.75$ .

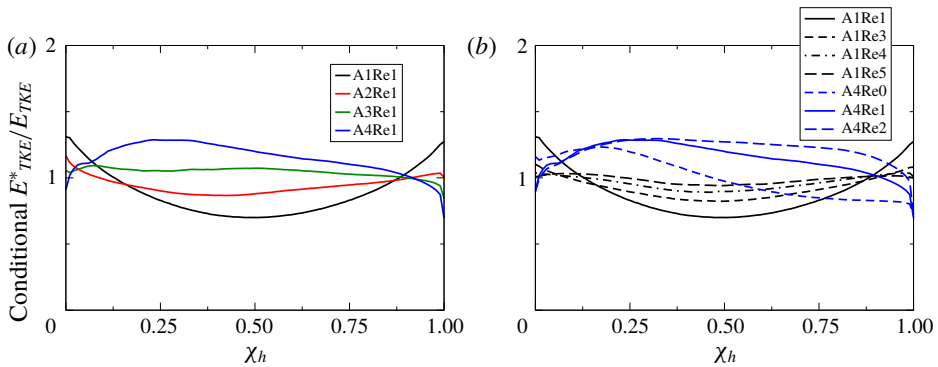


FIGURE 19. Atwood- and Reynolds-numbers effects on conditional expectation of  $E_{TKE}$  during saturated growth regime (at  $t/t_r = 1.75$ ).

An increase in  $Re_0$  reduces the asymmetry of conditional expectation. For the higher  $A$ -number cases, the conditional p.d.f. converges at the lighter-fluid side. This observation is consistent with the notion of mixing transition occurring at earlier times within the lighter-fluid regions compared to the heavier-fluid regions.

#### Conditional expectation of dissipation of $E_{TKE}$

The conditional expectation of the  $E_{TKE}$  dissipation remains asymmetric at high  $A$  during this regime, similar to the explosive growth regime (figure 20). Local dissipation expectations (computed for the specific density values) continue to take much larger values over mean dissipation values for higher  $A$  and  $Re_0$  numbers. For example, the largest conditional expectation of  $E_{TKE}$  dissipation is  $\approx 3$  for the A4Re2 case and is  $\approx 3.8$  for the A1Re5 case. However,  $Re_i$  effects decrease during the saturated growth. Furthermore,  $Re_0$  effects on the peak of the conditional mean are smaller for the higher- $A$ -number cases. This might be attributed to the location of the peak, which is within the lighter-fluid regions, where the mixing transition occurs relatively earlier than for the fully mixed and heavier-fluid regions.

#### Conditional expectation of enstrophy

The conditional expectation of enstrophy is shown in figure 21(a,b); the vertical, horizontal and total components are plotted for comparison. The conditional



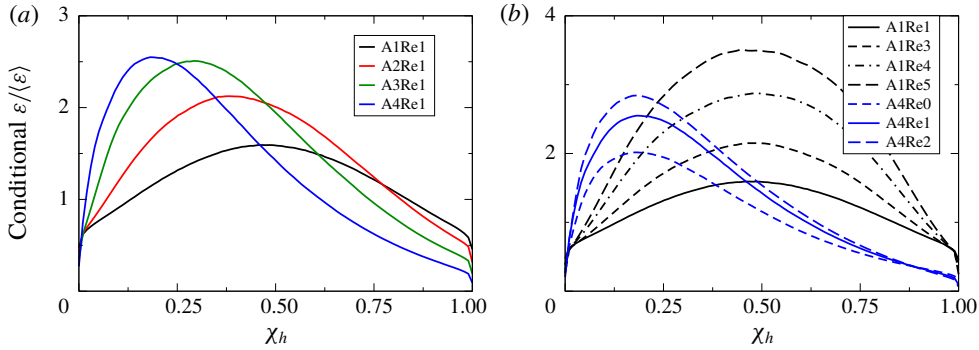


FIGURE 20. Atwood- and Reynolds-numbers effects on conditional expectation of  $E_{TKE}$  dissipation during saturated growth regime (at  $t/t_r = 1.75$ ).

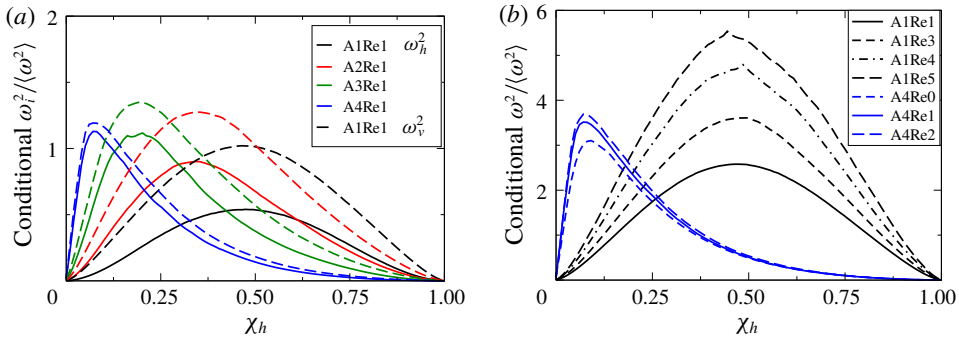


FIGURE 21. Atwood- and Reynolds-numbers effects on conditional expectation of (a) vertical ( $\omega_v^2 = \omega_1^2$ ) and horizontal ( $\omega_h^2 = (\omega_2^2 + \omega_3^2)/2$ ) enstrophy components and (b) total enstrophy during saturated growth regime (at  $t/t_r = 1.75$ ).

expectation remains strongly skewed towards the light-fluid regions for the high- $A$ -number cases, similar to observations reported for the explosive growth. The main difference observed in the saturated growth (compared to explosive growth) regime is that the enstrophy becomes almost isotropic at  $t/t_r = 1.75$  at the highest  $A$  number. Additionally, for the high- $A$ -number cases ( $A \geq 0.5$ ),  $Re_0$  effects become weaker, similar to the behaviour of the conditional expectation of the dissipation of  $E_{TKE}$ . Interestingly, different rates of convergence with  $Re_0$  are observed for the different metrics discussed in this section. For example, at  $t/t_r = 1.75$ , the velocity p.d.f. is substantially converged for all the cases reported (not shown here). However, the conditional expectation of  $E_{TKE}$  is weakly converged for the high- $Re_0$  cases, while the conditional expectations of dissipation and enstrophy are further away from convergence.

### 4.3. Fast decay

The fast decay regime starts when dissipation of  $E_{TKE}$  begins to overcome  $E_{TKE}$  generation. Since the rate of molecular mixing is high and buoyancy forces decay rapidly, the rate of  $E_{TKE}$  decay increases with time such that  $d^2 E_{TKE}/dt^2 < 0$ . During this regime, similarities are observed with RTI under reversed acceleration  $g \leq 0$ . In

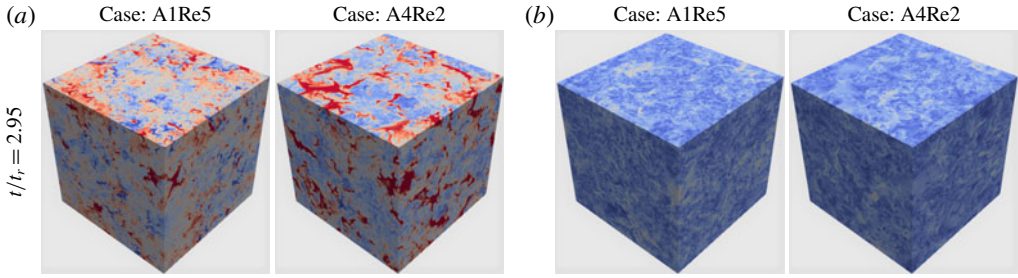


FIGURE 22. Three-dimensional visualization of (a) the mole fraction and (b) the velocity magnitude ( $\sqrt{u_1^2 + u_2^2 + u_3^2}$ ) for the cases  $A = 0.05$  (A1Re5) and  $A = 0.75$  (A4Re2) are displayed at  $t/t_r = 2.95$ .

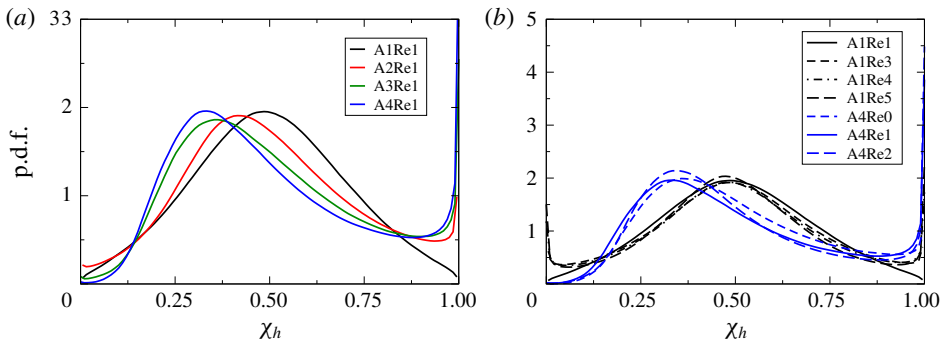


FIGURE 23. The p.d.f. of the density field for the different (a)  $A$  and (b)  $Re_0$  values at  $t/t_r = 2.95$ .

HVDT, partially mixed fluids become well mixed within the flow and turbulence starts to decay similar to observations in RTI with acceleration reversal that makes the global flow stable with the presence of local fluid patches that are unstable due to the stirring (see figure 22). These local fluid patches assist the turbulence decay due to local (but limited) turbulence generation (Ramaprabhu *et al.* 2013; Aslangil *et al.* 2016). Furthermore, this regime also has some similarities with shock-driven RMI. In RMI, VD turbulence generated due to the shock decays purely as there is no buoyancy assistance. However, the VD mixing physics is similar in both flows as turbulent fluid patches with different densities mix efficiently during  $E_{TKE}$  decay.

#### 4.3.1. Atwood-number effects on p.d.f. evolutions

##### Density p.d.f.

During fast decay, the density p.d.f. is highly asymmetric for large- $A$ -number cases. A closer look at the tails of the distribution shows very little amounts of pure light fluid left in the flow. However, there are still substantial amounts of pure heavy fluid within the flow (see figure 23a). The normalized skewness ( $S_k$ ), which identifies the asymmetry level of the p.d.f. distribution and takes positive values for the p.d.f.s with longer right-side tails and negative values for the p.d.f.s with longer left-side tails, is

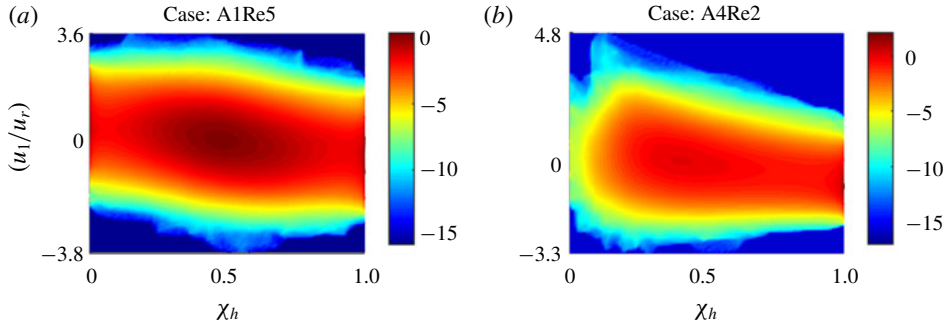


FIGURE 24. Normalized jMDFs ( $\log(\mathcal{F}/\bar{\rho})$ ) for (a)  $A = 0.05$  (A1Re5) and (b)  $A = 0.75$  (A4Re2) cases displayed at  $t/t_r = 2.95$ .

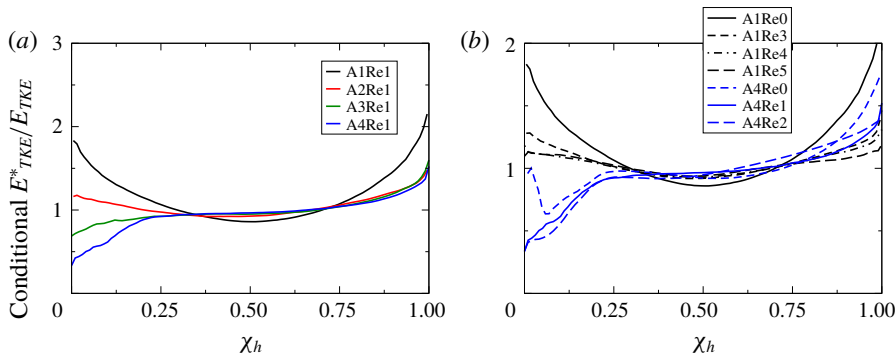


FIGURE 25. Atwood- and Reynolds-numbers effects on conditional expectation of  $E_{TKE}$  during fast decay regime (at  $t/t_r = 2.95$ ).

defined as (Ristorcelli & Clark 2004)

$$S_k = \frac{\langle \rho^3 \rangle}{\langle \rho^2 \rangle^{3/2}}. \tag{4.1}$$

Normalized skewness takes its maximum values during the fast decay regime. The  $S_k$  value tends to slightly increase upon increasing  $Re_0$ . For all  $A$ -number cases (the moderate cases are not shown), the  $Re_0$ -number effect is weak during the fast decay, indicating that this quantity reaches the fully developed stage.

*Velocity–density jMDF*

The jMDF variations for lowest and highest  $A$  numbers are shown in figure 24. As can be seen, in contrast to the density p.d.f., the asymmetry of the jMDF at each density level tends to decrease, as  $P_i$  and variability in  $1/\rho^*$  are lower due to mixing. However, the jMDFs are still significantly different for low- and high- $A$ -number cases. Thus, for the high- $A$  case, there are still significant large positive velocity events. Moreover, due to the existence of large amounts of pure heavy fluid for high- $A$ -number cases, the jMDF peaks in two regions, one close to the mean density value and near zero vertical velocity, and the other at the heaviest fluid region and slightly negative vertical velocity.

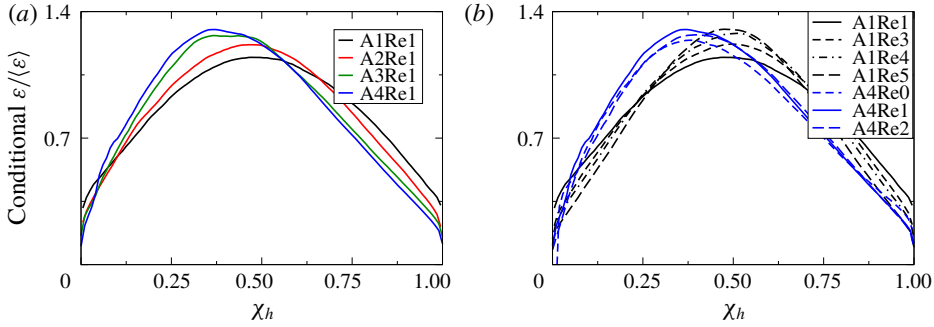


FIGURE 26. Atwood- and Reynolds-numbers effects on conditional expectation of  $E_{TKE}$  dissipation during fast decay regime (at  $t/t_r = 2.95$ ).

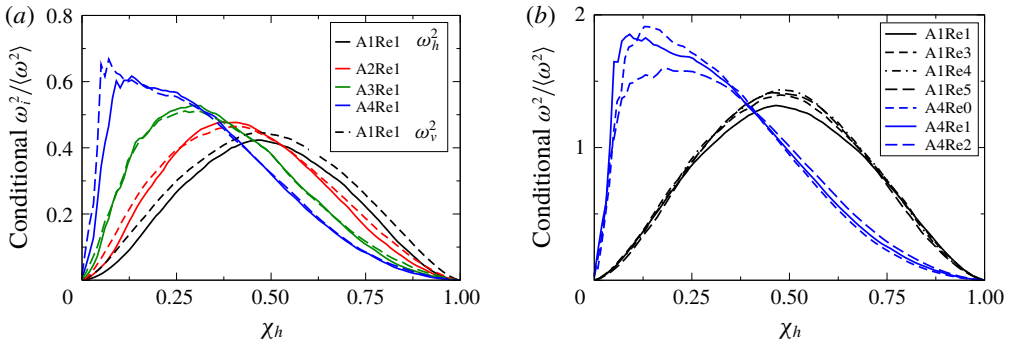


FIGURE 27. Atwood- and Reynolds-numbers effects on conditional expectation of (a) vertical ( $\omega_v^2 = \omega_1^2$ ) and horizontal ( $\omega_h^2 = (\omega_2^2 + \omega_3^2)/2$ ) entrophy components and (b) total entrophy during fast decay regime at  $t/t_r = 2.95$ .

4.3.2. Conditional expectations

*Conditional expectation of  $E_{TKE}$*

During fast decay,  $A$  number continues to play an important role on the behaviour of the conditional expectation of  $E_{TKE}$ . The light- and heavy-fluid regions have larger  $E_{TKE}$  values for the lower- $A$ -number cases, as these regions continue to move faster. However, for high  $A$  numbers, the average  $E_{TKE}$  values increase slightly within the heavier-fluid regions (see figure 25).

*Conditional expectation of  $E_{TKE}$  dissipation*

During fast decay, the conditional mean of dissipation becomes independent of  $Re_0$ . In addition, the  $A$ -number effect becomes weak for the range investigated here. The energy mostly dissipates within flow regions that are fully mixed and the local values are no longer much larger than the mean values (see figure 26).

*Conditional expectation of entrophy*

In contrast to the dissipation field, the conditional entrophy is still dependent on  $A$  as shown in figure 27. Similar to the dissipation field, the local values are closer to the whole-domain average for all cases and  $Re_0$  effects are not significant. It is also noticeable that the components of the entrophy field are similar, which indicates small-scale isotropy during this regime.

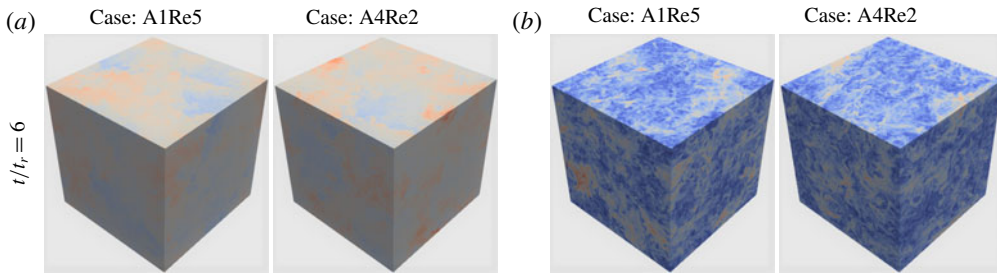


FIGURE 28. Three-dimensional visualization of (a) the mole fraction and (b) the velocity magnitude ( $\sqrt{u_1^2 + u_2^2 + u_3^2}$ ) for  $A = 0.05$  case (A1Re5) and  $A = 0.75$  case (A4Re2) displayed at  $t/t_r \approx 6$ .

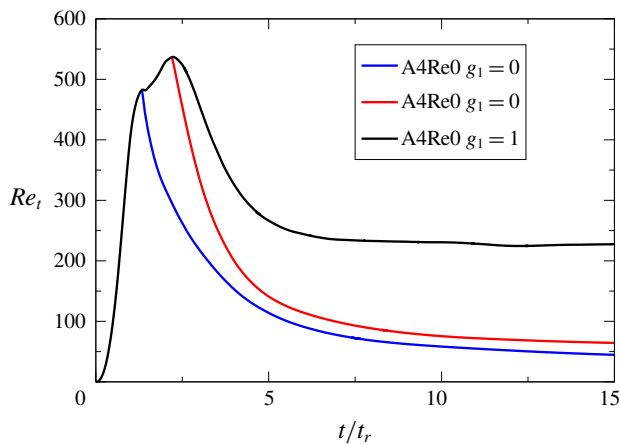


FIGURE 29. Reynolds-number evolution for pure and buoyancy-assisted decays.

#### 4.4. Gradual decay

After the period of fast decay, the flows settle into a late-time slow decay regime, as  $d^2 E_{TKE}/dt^2$  again becomes larger than zero. This regime has some similarities with the core of the mixing region at late time of the RMI and RTI under reversed acceleration ( $g \leq 0$ ). Buoyancy forces continue to weaken and no pure fluids exist within the flow. In addition, as most of the fluids have been molecularly mixed ( $\theta > 0.95$  for all cases), the VD effects are weak during gradual decay, which makes HVDT comparable to the study by Batchelor *et al.* (1992). Figure 2 shows that HVDT attains a non-decaying Reynolds-number behaviour during the late-time stage. An interesting comparison can be made between the case of buoyancy-assisted decay and pure decay (where  $g_i$  is set to zero at some time instant). As can be seen in figure 29, in the case of pure decay, the  $Re_t$  number decreases continuously. However, when the decay is assisted by buoyancy forces, the Reynolds number does not decrease. This is consistent with the theoretical analysis of Batchelor *et al.* (1992), which highlights the importance of density fluctuations in the infrared part of the energy spectrum, even as they asymptotically decrease to zero. In this study, we aim to reach as high a  $Re_t$  value as possible during the flow evolution, so the initial peak of the density spectrum is chosen to be at low wavenumbers. Unfortunately,

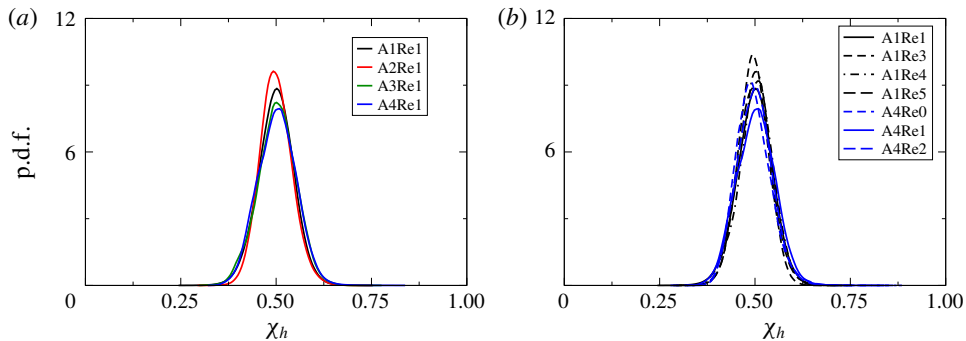


FIGURE 30. The p.d.f. of the normalized density field for different (a)  $A$  numbers and (b)  $Re_t$  numbers at  $t/t_r \approx 6$ .

this choice of initial conditions leads to insufficient infrared part in the spectra to be able to draw definitive conclusions about the decay laws of  $E_\rho$  and  $E_{TKE}$  and the behaviour of  $Re_t$ . Shifting the peak of the initial density energy spectrum to higher wavenumbers, while maintaining  $Re_t$  number above the mixing transition, would require much larger resolutions and is outside the scope of the current work.

During the gradual decay regime, as the turbulent kinetic energy behaviour no longer changes, the flow also reaches a self-similar behaviour. Thus, density and velocity p.d.f.s tend to reach symmetric shape for all  $A$  numbers investigated here. Gradual decay has strong similarities with sufficiently developed RTI under negative (reversed) acceleration where the flow is stably stratified and is not fed by pure fluids (Aslangil *et al.* 2016). Similarly, with HVDT during gradual decay, the flow tends to become fully mixed under the presence of weak buoyancy forces primarily due to the buoyancy differences between the partially mixed regions (Livescu & Wei 2012; Ramaprabhu *et al.* 2013; Aslangil *et al.* 2016). Gradual decay also has similarities with atmospheric and oceanic flows where the flow perturbed by different sources may decay under weak buoyancy forces.

#### 4.4.1. Atwood-number effects on p.d.f. evolutions

##### Density p.d.f.

During gradual decay, as most of the fluids are mixed, the density p.d.f. is accumulated at around mean density (see figure 30). Both  $A$ - and  $Re_0$ -number effects are limited during this regime; however, the density p.d.f. tail is slightly longer at the heavy-fluid side for larger  $Re_0$  and  $A$  numbers.

##### Velocity–density jMDF

The jMDFs of density and velocity fields (see figure 31) become closer for the low- and high-Atwood-number cases. The slightly tilted behaviour indicates that during decay, velocity and density fields remain (weakly) negatively correlated. Heavier regions moving close to the maximum downward velocities are still present in the high- $A$ -number case, while slightly larger maximum vertical velocities indicate that still the light-fluid regions continue to be more stirred by turbulence.

#### 4.4.2. Conditional expectations

During gradual decay, the conditional means of  $E_{TKE}$ , dissipation of  $E_{TKE}$  and enstrophy become less dependent on  $Re_0$  and  $A$  numbers. For all  $A$  numbers studied

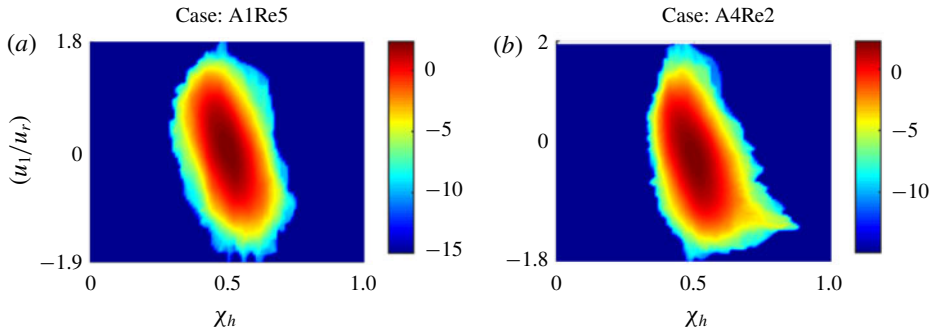


FIGURE 31. Normalized jMDFs ( $\log(\mathcal{F}/\bar{\rho})$ ) for (a)  $A = 0.05$  (A1Re5) and (b)  $A = 0.75$  (A4Re2) cases displayed at  $t/t_r \approx 6$ .

here,  $E_{TKE}$  is slightly larger within the lightest and heaviest flow regions as buoyancy forces are still present compared to the fully mixed flow (see figure 32a). Moreover, all three quantities have values close to their means in well-mixed regions, showing the importance of these regions to the global statistics. However, a lot of variability is still observed in lighter- and heavier-than-average fluid regions. In particular, while dissipation fluctuates and tends to be lower than average in light- and heavy-fluid regions, enstrophy tends to be lower than average in heavy-fluid regions, but higher than average in light-fluid regions for larger  $A$  (see figure 32b,c). Thus, even at late times, lighter-fluid pockets maintain stronger vortical motions, whereas in heavier-fluid regions vorticity can become small.

### 5. Spectral evolution of buoyancy-driven VDT

For variable-density flows, there is no unique way to define a kinetic energy spectrum. Quadratic expressions with the same units can be constructed from kinetic energy definitions per unit mass, i.e.  $\text{TKE}^I \equiv \langle |\sqrt{\bar{\rho}} \mathbf{u}''|^2 \rangle$ , or per unit volume, i.e.  $\text{TKE}^{II} \equiv \langle |\sqrt{\rho^*} \mathbf{u}''|^2 \rangle$  (Kida & Orszag 1990; Cook & Zhou 2002; Livescu & Ristorcelli 2008). Non-quadratic forms can also be constructed, using products between momentum per unit volume,  $\rho^* \mathbf{u}''$ , or per unit mass,  $\mathbf{u}''$  (Clark & Spitz 2005; Lai, Charonko & Prestridge 2018; Pal *et al.* 2018). However, in order for the kinetic energy spectrum to develop an inertial range, the viscous effects need to be restricted to the small scales. For VD turbulence, such scale decomposition is not as straightforward as in incompressible flows. In particular, it is possible that certain quantities exhibit viscous effects at all scales, while others do not (Zhao & Aluie 2018). Using a coarse-grained filtering, Zhao & Aluie (2018) showed that the filtered Favre TKE has the property that viscous effects vanish at large scales for sufficiently large Reynolds numbers, which they called the inviscid-scale decomposition criterion. The filtered forms of kinetic energies  $\text{TKE}^I$  and  $\text{TKE}^{II}$  do not have this property, when the density variations are large. These considerations fully apply only when the viscosity is constant. The variable-viscosity case does not satisfy an inviscid-scale decomposition criterion for arbitrary variations of viscosity with density. While it is outside the goals of the paper to discuss this general case, here we explore several forms of the velocity power spectra.

A quadratic form of the TKE that satisfies the inviscid-scale decomposition criterion for constant viscosity is proposed here as  $\text{TKE}^{III} \equiv \langle |\rho^* \mathbf{u}'' / \sqrt{\bar{\rho}}|^2 \rangle$ . Table 2 lists two

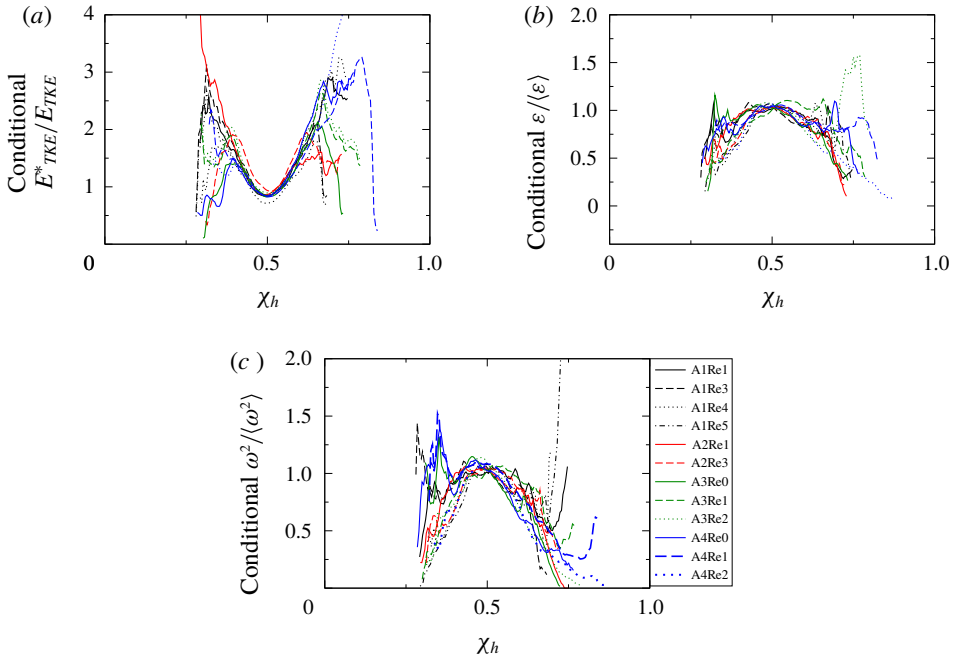


FIGURE 32. Atwood- and Reynolds-numbers effects on conditional expectation of normalized (a)  $E_{TKE}$ , (b)  $E_{TKE}$  dissipation and (c) total enstrophy during gradual decay (at  $t/t_r \approx 6$ ).

commonly used definitions together with the new energy form and the viscous terms in the corresponding spectral transport equations, where  $\hat{\cdot}$  denotes a Fourier transform and  $\dagger$  the complex conjugate. As shown by Zhao & Aluie (2018), terms of the type  $\tau_{ij,j}/\rho^*$  or  $\tau_{ij,j}/\sqrt{\rho^*}$  cannot be proven to decrease at large scales for sufficiently large density variations. Such terms appear in the spectral transport equations for  $TKE^I$  and  $TKE^{II}$ , so it is expected that these kinetic energies will have viscous contributions at all scales in VD turbulence. Similar terms also appear in the spectral transport equations for the non-quadratic forms of the kinetic energy used in the literature. On the other hand, the viscous term in the spectral transport equation for  $TKE^{III}$  is expected to vanish at large scales (for constant viscosity), irrespective of the  $A$  number.

Figure 33 presents the compensated energy spectra calculated based on the  $TKE^I$ ,  $TKE^{II}$  and  $TKE^{III}$  definitions; case A4Re2 is chosen for illustration. The spectra are plotted at the end of the saturated growth, where production and dissipation are equal. As can be seen in figure 33, the large scales are suppressed for definitions I and II and they have a flatter slope than the classical  $-5/3$  slope. The differences are small for definition II for the range of density variations considered, as these are attenuated by the square root. In addition, figure 34 plots the corresponding viscous term for each energy spectrum option. The viscous term for the new definition  $TKE^{III}$  is smaller for the entire range; more importantly, the viscous effects decay at large scales. However, the viscous terms estimated using the definitions I and II continue to affect the evolution of large scales. This leads to a relative suppression of the large scales and a flatter slope than  $-5/3$ , which is consistent with findings by Zhao & Aluie (2018). As the  $A$  number decreases and the flow becomes Boussinesq, the



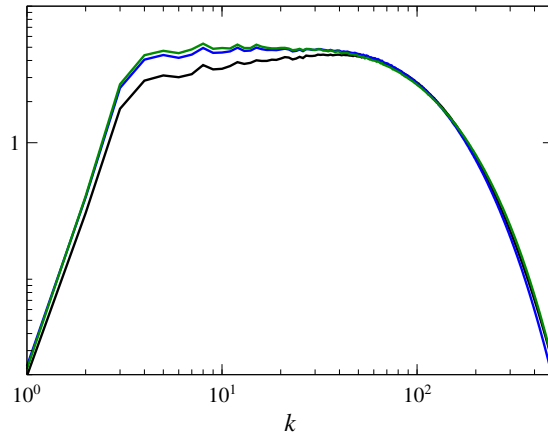


FIGURE 33. Comparison of the compensated energy spectrum ( $E_k k^{5/3}$ ) calculated based on  $TKE^I$  (black line),  $TKE^{II}$  (blue line) and  $TKE^{III}$  (green line) for the A4Re2 case at the start of fast decay at  $t/t_r = 2.35$ .

Options	Formula	Corresponding spectral viscous term
$TKE^I$	$\langle  \sqrt{\bar{\rho}} \mathbf{u}' ^2 \rangle$	$(\widehat{\sqrt{\bar{\rho}} u'_i})^\dagger (\widehat{\sqrt{\bar{\rho}} \tau_{ij,j} / \rho^*}) + (\widehat{\sqrt{\bar{\rho}} u'_i / \sqrt{\bar{\rho}}}) (\widehat{\sqrt{\bar{\rho}} \tau_{ij,j} / \rho^*})^\dagger$
$TKE^{II}$	$\langle  \sqrt{\rho^*} \mathbf{u}'' ^2 \rangle$	$(\widehat{\sqrt{\rho^*} u''_i})^\dagger (\widehat{\tau_{ij,j} / \sqrt{\rho^*}}) + (\widehat{\sqrt{\rho^*} u''_i}) (\widehat{\tau_{ij,j} / \sqrt{\rho^*}})^\dagger$
$TKE^{III}$	$\langle  \rho^* \mathbf{u}'' / \sqrt{\bar{\rho}} ^2 \rangle$	$(\widehat{\rho^* u''_i / \sqrt{\bar{\rho}}})^\dagger (\widehat{\tau_{ij,j} / \sqrt{\bar{\rho}}}) + (\widehat{\rho^* u''_i / \sqrt{\bar{\rho}}}) (\widehat{\tau_{ij,j} / \sqrt{\bar{\rho}}})^\dagger$

TABLE 2. Different approaches to calculate VD kinetic energy spectra. Only the new form proposed here,  $TKE^{III}$ , has a viscous term in its corresponding spectral transport equation that vanishes at large scale for large density variations.

density fluctuations also decrease and all three definitions give similar spectra. For strongly variable-density flows with variable viscosity coefficient, there is no general methodology to construct a quadratic energy form which ensures that viscous effects remain confined at small scales. While  $TKE^{III}$  only has the property that the viscous effects vanish at large scales for the constant-viscosity case, the results show that it is a better choice to examine the kinetic energy spectrum than  $TKE^I$  and  $TKE^{II}$  for the cases considered here.

### 5.1. Spectral energy evolution

As the flow undergoes rapid changes at early times and transitions from TKE growth to decay, it is expected that the energy spectrum follows a complex evolution. In particular, the shape of the spectrum at early times should be strongly dependent on the production term, while at late times, during gradual decay, it should relax to fully developed conditions. In the previous section, a new quadratic form of the TKE was shown to have reduced viscous effects at large scales for the cases considered here, while for the constant-viscosity case those effects should vanish at large scales. This form, i.e.  $TKE^{III}$ , is used throughout this section.

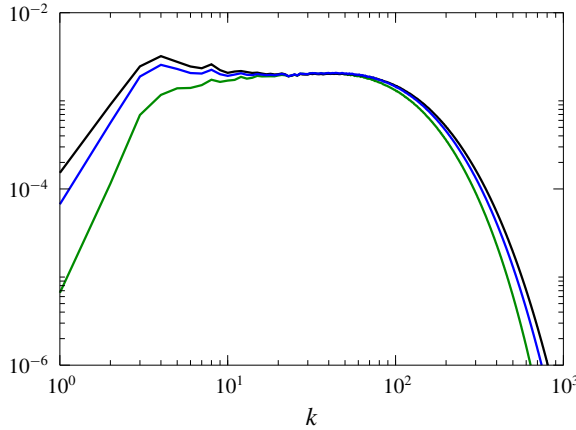


FIGURE 34. Comparison of the viscous terms in the spectral transport equations for  $TKE^I$  (blue line),  $TKE^{II}$  (green line) and  $TKE^{III}$  (black line) for the A4Re2 case at  $t/t_r = 2.35$ . The values are multiplied by constants such that the viscous terms have the same magnitudes at  $k = 50$  for clarity.

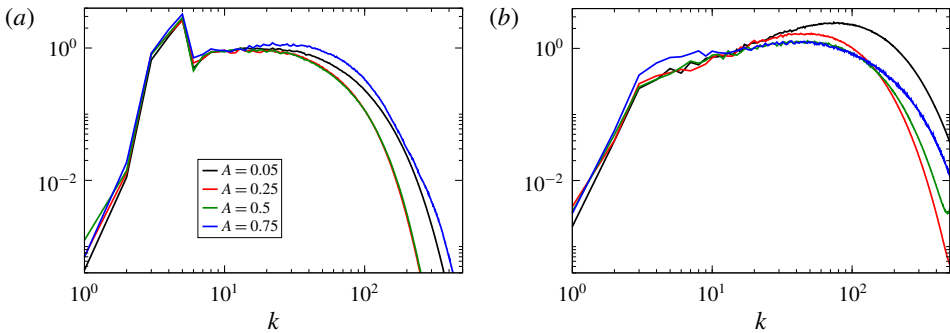


FIGURE 35. Compensated spectra of the normalized mass flux ( $a_1(k)k^{7/3}/(A\bar{\rho}U_r)$ ) for different  $A$  numbers at (a)  $t/t_r = 1.15$  and (b)  $t/t_r = 2.35$ .

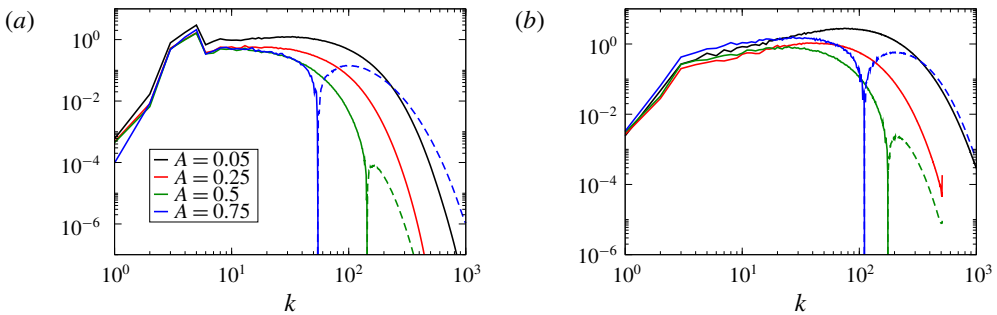


FIGURE 36. Compensated spectra of the normalized production term for  $TKE^{III}$  option ( $P_{TKE^{III}} = P_{,1}u_1''\rho^*\rho/(4\bar{\rho}A^2)k^{7/3}$ ) for different  $A$  numbers at (a)  $t/t_r = 1.15$  and (b)  $t/t_r = 2.35$ . Dashed lines represent negative  $P_{TKE^{III}}$ .

For the Boussinesq limit, the buoyancy-production term, which is proportional to the mass flux ( $\rho^*u_1$  from (2.15)) has been reported to have  $-7/3$  slope in the inertial range (Lumley 1967); similar observations have also been made in a stationary version of HVDT (Chung & Pullin 2010). Figure 35 presents the mass flux spectra (normalized by  $A\bar{\rho}U_r$ ) for different  $A$  numbers at the start of the saturated growth  $t/t_r = 1.2$  and fast decay  $t/t_r = 2.4$  regimes. The data are consistent with previous studies as the mass flux has  $-7/3$  slope at intermediate scales for all  $A$  numbers. At early times, the  $-7/3$  slope covers a relatively wide range of scales at low  $A$  number. However, upon an increase in  $A$  number, the mass flux spectrum has a sharper decay at small scales and the  $-7/3$  slope is restricted to a shorter range of scales. As turbulence starts to decay though, the  $-7/3$  slope moves to higher wavenumbers and becomes restricted to a shorter range of scales at lower  $A$  number (figure 35*b*). This behaviour underlies the non-monotonic dependence of the flow evolution on the  $A$  number. As the  $A$  number is increased, the light- and heavy-fluid regions are accelerated faster, which increases the stirring, and ultimately leads to faster molecular mixing.

For the  $TKE^{III}$  definition, the production term,  $P_{TKE^{III}}$ , is different from the mass flux and is proportional to  $P_{,1}\rho u_1''\rho^*$ . Figure 36 presents the spectrum of  $P_{TKE^{III}}$ , normalized by  $4\bar{\rho}A^2$ . At small  $A$  numbers,  $P_{TKE^{III}}$  spectral shapes are close to those of the mass flux. However, at larger  $A$  numbers, the production term quickly decreases at intermediate scales and even becomes negative at very small scales. This behaviour can be related to the weighting with the instantaneous density compared to the mass flux. At large scales, both the heavy- and light-fluid regions move coherently in the direction of and opposite to gravity, respectively. Thus,  $u''$  and  $\rho$  have opposite signs and, since the mean pressure gradient is negative, the contributions to the production are positive in both heavy- and light-fluid regions. However, at early times, the mixing layers between pure-fluid regions contain significant inversion regions, where  $u''$  and  $\rho$  have the same sign, resulting in negative production term at small scales. As the stirring encompasses the whole flow and the pure-fluid regions vanish in the later stages of the flow development, the production term becomes positive at all scales (not shown).

At all  $A$  numbers, during explosive growth, the production term dominates the spectral kinetic energy balance, and the TKE develops a  $-7/3$  slope (see figure 37). This slope extends over a larger range for  $A = 0.75$  during this regime; however, the lower- $A$ -number results again underlie the non-monotonic dependence on  $A$  number.

Subsequently, during the saturated growth, due to the enhanced molecular mixing, the production term starts to weaken and the production-to-dissipation ratio decays to a value of 1. As the equilibration between TKE production and dissipation occurs, the kinetic energy spectrum transitions from a  $-7/3$  slope at intermediate scales, to a  $-5/3$  slope for all  $A$  numbers (see figure 38). The fast decay represents a transition period from evolving turbulence to fully developed turbulence. While at the beginning of this regime the  $-5/3$  slope extends over a large range of scales, this is not the fully developed spectral shape. Indeed, the upper intermediate scales are still evolving and reach a  $-1$  slope at the end of this regime. However, the Kolmogorov mechanism dominates the lower intermediate scales of the flow and they retain the  $-5/3$  slope (see figure 39). Furthermore, for the higher-resolution DNS ( $1024^3$  and  $2048^3$ ), which reach higher values of  $Re_t$  and thus a better separation between the energetic and dissipation scales, we observe a longer range of scales that have a slope of  $-5/3$  at the end of the fast decay regime. During gradual decay, the spectral shape remains very similar as seen in figure 40, indicating that the flow has reached

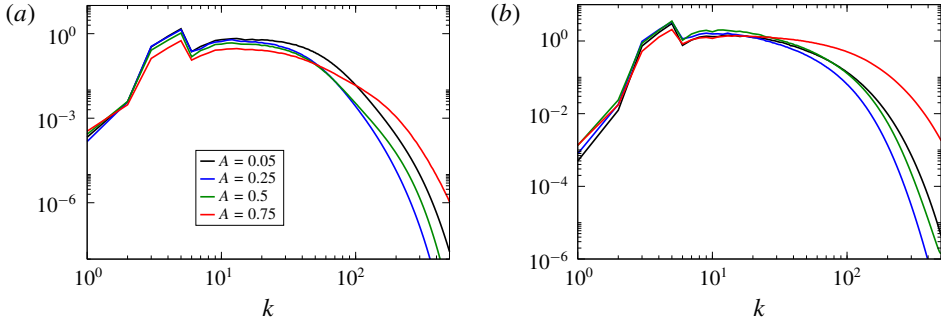


FIGURE 37. Compensated energy spectra  $E(k)k^{7/3}$  for different  $A$  numbers (a) during explosive growth at  $t/t_r = 0.65$  and (b) at beginning of saturated growth at  $t/t_r = 1.15$ .

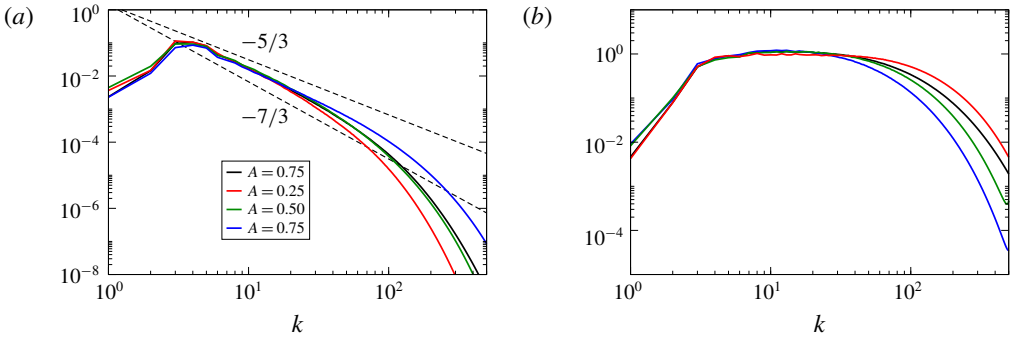


FIGURE 38. Energy spectra for different  $A$  numbers (a) during saturated growth at  $t/t_r = 1.75$  and (b) at beginning of fast decay at  $t/t_r = 2.35$  ( $E(k)k^{5/3}$ ).

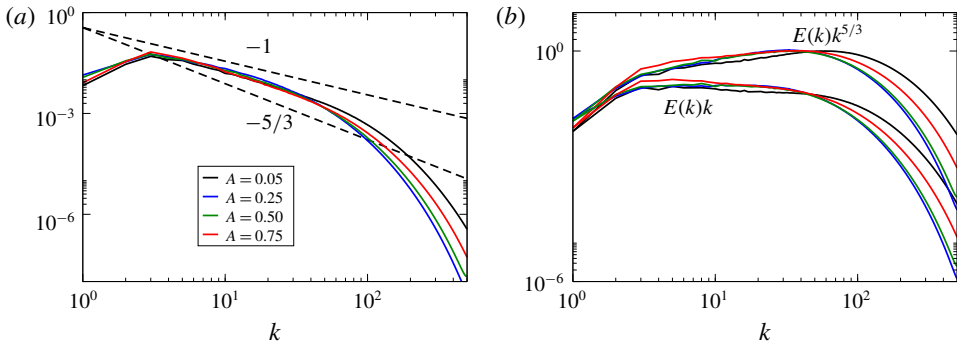


FIGURE 39. Energy spectra for different  $A$  numbers during fast decay at (a)  $t/t_r = 2.95$  and (b)  $t/t_r = 3.35$ .

its fully developed state. Similar results are reported by Batchelor *et al.* (1992) for their energy spectra of the Boussinesq case as well.

Several studies of buoyancy-driven turbulence have reported flatter slopes than  $-5/3$  at intermediate scales. For example, Gat *et al.* (2017) reported a  $-4/3$  slope in their study of a buoyancy-driven shear flow. They attributed this flatter slope to the

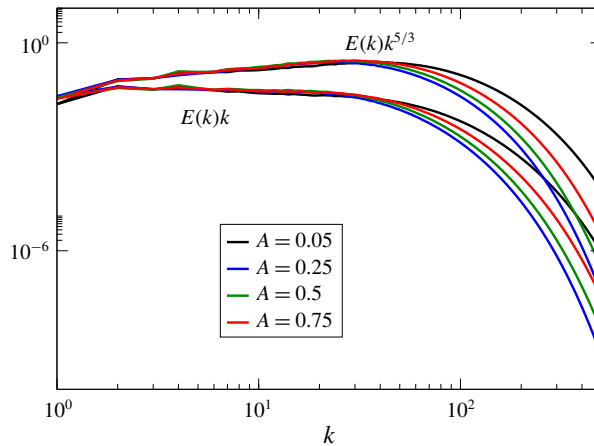


FIGURE 40. Energy spectra for different  $A$  numbers during gradual decay at  $t/t_r = 6$ .

turbulence intermittency; however, we believe that the presence of buoyancy causes the emergence of two spectral ranges at intermediate scales, with a  $-5/3$  slope at smaller intermediate scales and a flatter slope at larger scales due to the assistance of buoyancy production.

### 5.2. Spectral anisotropy

The Reynolds stress anisotropy tensor ( $B_{ij}$ ) is defined here consistent with the TKE expression as

$$B_{ij} = \frac{\langle (\rho^* u_i'') (\rho^* u_j'') \rangle}{\langle (\rho^* u_i'') (\rho^* u_i'') \rangle}. \tag{5.1}$$

For isotropic turbulence,  $B_{11} = B_{22} = B_{33} = 1/3$ , while the maximum value of each component is 1. To investigate the scale dependence of the normal stress anisotropy, the definition above is extended using the kinetic energy spectrum in each direction. Owing to the presence of energy production, it is expected that the large scales remain anisotropic. This influence extends deep into the intermediate scales (Soulard & Griffond 2012). However, at sufficiently large  $Re_t$ , the spectrum should become broad enough that the influence of energy production vanishes at high enough wavenumbers, so that a classical inertial range may emerge. However, under strongly non-equilibrium conditions, this picture might not hold. In particular, it is possible that the dissipation range may become anisotropic even when intermediate scales are isotropic. Thus, Livescu & Ristorcelli (2008) showed a direct connection between the large and dissipation scales during the growth of HVDT at small to moderate  $A$ . This finding was later confirmed in a stationary but inhomogeneous version of the flow with a non-zero mean density gradient (Chung & Pullin 2010). Here, we explore the Atwood- and Reynolds-numbers effects on this anisotropic behaviour of intermediate and viscous ranges during the growth and decay regimes at higher Reynolds numbers and for a larger range of  $A$  numbers than Livescu & Ristorcelli (2008).

Figure 41 shows the vertical component of the anisotropy tensor for different  $A$  and  $Re_0$  numbers as a function of the wavenumber during explosive growth. Owing to the much larger  $E_{TKE}$  production than  $E_{TKE}$  dissipation, the kinetic energy spectrum is dominated by the production term and the flow is anisotropic at all scales. Up to

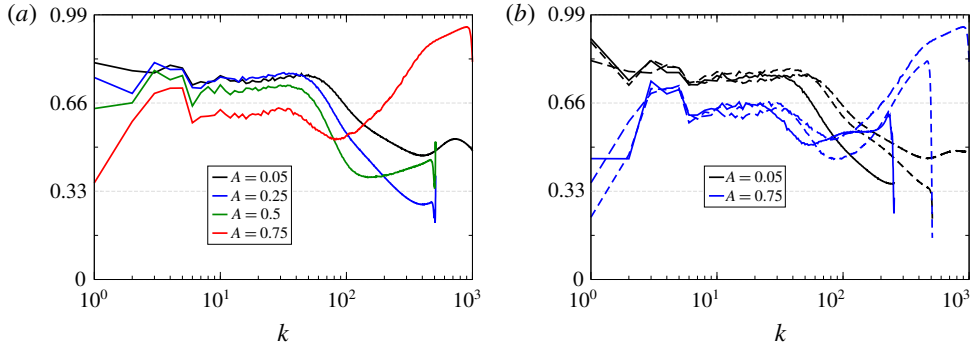


FIGURE 41. Vertical component of the anisotropy tensor as a function of the wavenumber for different (a)  $A$  and (b)  $Re_0$  numbers during explosive growth at  $t/t_r = 0.65$ . In (b), longer spectrum ranges correspond to higher-resolution and higher-Reynolds-number cases.

about  $k \sim 60$ , the vertical component has as much energy as the horizontal components combined, similar with the overall anisotropy of the flow. While the normal stress anisotropy decreases for larger wavenumbers, it remains significant in the viscous range, especially at  $A = 0.75$ , where it reaches higher levels than at large scales. Increasing  $Re_0$  has a relatively minor influence on the normal stress anisotropy, and the viscous range anisotropy extends to the smallest scales of the flow.

Furthermore, compared to the cases with lower  $A$  numbers, cases with larger  $A$  numbers have lower anisotropy values at large scales. This observation is consistent with the  $E_{TKE}$  conversion rates, which decrease upon increase in  $A$  number. The  $E_{TKE}$  production-to-dissipation ( $P/D$ ) ratio is lower for the higher- $A$ -number cases, which reduces the anisotropy levels at intermediate scales.

As the flow develops during the saturated growth and the  $P/D$  ratio decays, the nonlinear effects slowly start to dominate at intermediate scales, which become isotropic over all  $A$ - and  $Re_i$ -number cases reported in this paper (figure 42). However, there remains a persistent anisotropy in the viscous range, consistent with earlier studies (Livescu & Ristorcelli 2008). This anisotropy is higher at small  $A$  numbers, underlying the complex relation between stirring and mixing, as described throughout this paper. There seems to be a faster decrease of the anisotropy with the Reynolds number figure 42b), as the stronger stirring at early times leads to an accelerated increase in molecular mixing. The classical RTI problem or similar configuration cases where  $g > 0$  are the most common examples of  $P \geq D$  flows that exhibit viscous range anisotropy. Such results are also reported for the classical RTI problem (Livescu *et al.* 2009) from the DNS data of Cabot & Cook (2006).

During decay regimes, production is smaller than the total dissipation and the flow reaches its fully developed structure. Consistently, the normal stress anisotropy extends over the whole small-scale range (not shown).

### 5.3. Density spectra

The density energy spectra normalized by  $(A\bar{\rho})^2$ ,  $E_\rho(k)/(A\bar{\rho})^2$ , are shown in figure 43 for different  $A$  numbers. In this normalization, the density spectra collapse at large scales for all  $A$  numbers. During the explosive growth, the inertia associated with stirring is not sufficient to disturb the large scales of the flow as observed in figure 43(a). The initial shapes of the large structures are preserved for all  $A$  numbers,

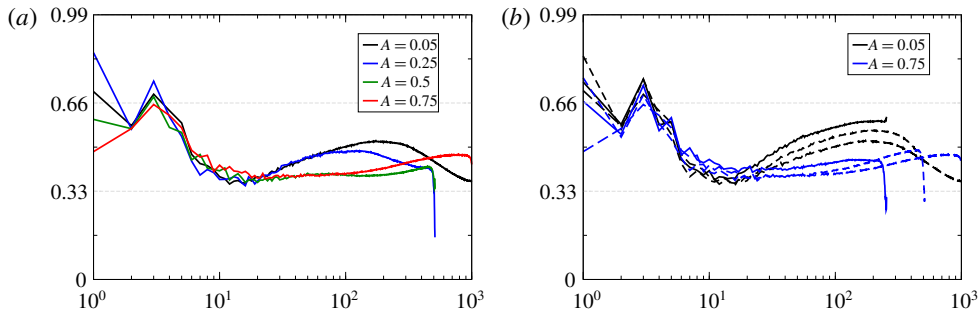


FIGURE 42. Vertical component of the anisotropy tensor as a function of the wavenumber for different (a)  $A$  and (b)  $Re_t$  numbers during saturated growth at  $t/t_r = 1.75$ .

as stirring and molecular mixing are mostly localized at the interface between the light- and heavy-fluid regions. This observation is also consistent with the evolution of the mole fraction shown in figure 6. As the flow transitions to saturated growth, the top-hat shape of the spectrum flattens out due to enhanced mixing (see figure 43*b*). The growth stages are followed by a fast decay where the top-hat shape of the density spectrum is removed and the spectra tend to become identical for all cases (see figure 43*c*). During late-time gradual decay, the slope of the density spectrum at large scales was observed to follow a  $k^{-1}$  power law; similar values were first reported by Lesieur & Rogallo (1989) for passive scalar mixing and later by Batchelor *et al.* (1992) for HVDT under Boussinesq assumption.

Even though different mixing rates are observed within different regions of the flow during both saturated growth and fast decay regimes, the density spectra are not able to capture this asymmetric behaviour; the evolution of the density spectrum is not affected by the asymmetric behaviour of the density p.d.f.

## 6. Conclusions

To better understand the variable-density effects, the highly non-equilibrium nature of HVDT is investigated by dividing the flow evolution into four different regimes based on the time derivatives of  $E_{TKE}$ . Table 3 presents the  $E_{TKE}$  behaviour during these four regimes. HVDT dynamics is also studied in detail by investigating the  $A$ - and  $Re_t$ -numbers effects during these four regimes; the unique characteristics that are observed are summarized below.

Most of the variable-density effects can be connected to different inertia of the light- and heavy-fluid regions, which makes them respond differently to changes in local strain. The inertia, in turn, changes the local stirring and, subsequently, the molecular mixing. Overall, the light-fluid regions not only develop more intense turbulence faster, but also mix faster. This complex asymmetric behaviour leads to non-monotonic flow development with respect to the Atwood number, as highlighted below.

### 6.1. Energy conversion rates

It is found that energy conversion rates strongly depend on density ratio of the mixing fluids. Cases with lower  $A$  numbers are more efficient to generate  $E_{TKE}$ ; however, all cases investigated are very efficient ( $\beta_{KE} > 0.9$ ) to generate  $E_{KE}$  during explosive

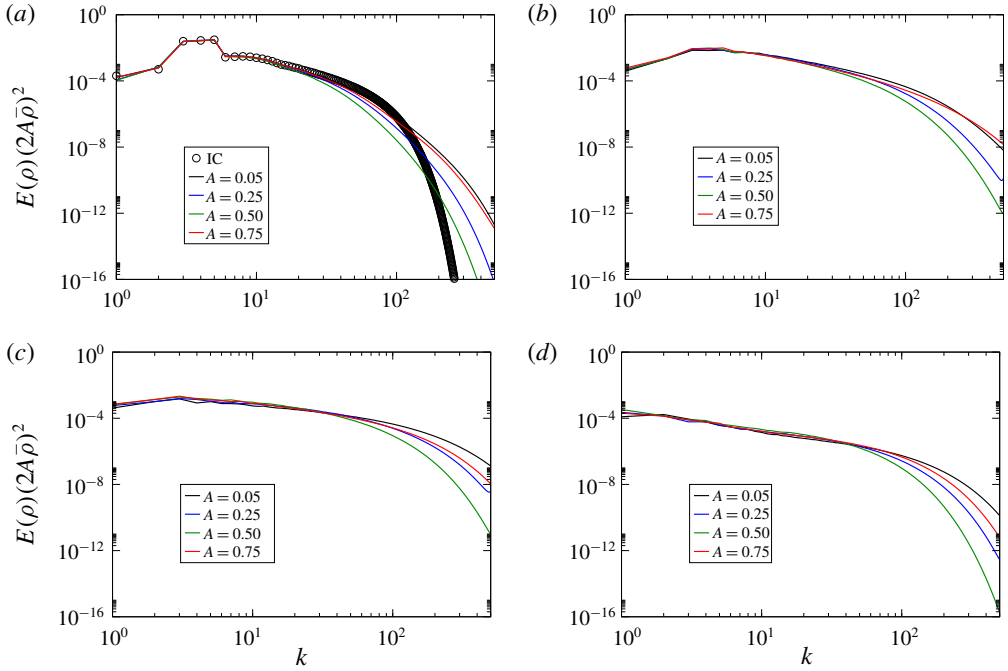


FIGURE 43. Normalized density energy spectra at (a)  $t/t_r = 0$  (IC = initial condition) and  $t/t_r = 0.65$  (explosive growth), (b)  $t/t_r = 1.75$  (saturated growth), (c)  $t/t_r = 2.95$  (fast decay) and (d)  $t/t_r = 6$  (gradual decay) for different  $A$  numbers.

---

Explosive growth	$\frac{dE_{TKE}}{dt} > 0$ and $\frac{d^2E_{TKE}}{dt^2} > 0$
Saturated growth	$\frac{dE_{TKE}}{dt} > 0$ and $\frac{d^2E_{TKE}}{dt^2} < 0$
Fast decay	$\frac{dE_{TKE}}{dt} < 0$ and $\frac{d^2E_{TKE}}{dt^2} < 0$
Gradual decay	$\frac{dE_{TKE}}{dt} < 0$ and $\frac{d^2E_{TKE}}{dt^2} > 0$

---

TABLE 3.  $E_{TKE}$  behaviour during different flow regimes.

growth. During saturated growth, the  $A$  number has a non-monotonic influence on the energy conversion ratio. Both  $E_{KE}$  and  $E_{TKE}$  conversion ratios peak at moderate  $A$ -number values between 0.25 and 0.5.

### 6.2. Asymmetric behaviour at high $A$ number

Mixing asymmetries that develop in buoyancy-driven HVDT were examined at high  $A$  and  $Re_i$  numbers. The velocity behaviour for high  $A$  numbers is different from cases with lower  $A$  numbers; different mixing rates are observed in flow regions



with different density levels. Owing to smaller inertia, lighter-fluid regions respond faster to changes in direction associated with stirring than heavier-fluid regions. In effect, the turbulent velocity fluctuations are larger in these regions. At  $A \geq 0.5$ , these asymmetries become noticeable, as observed in the jMDF of density and velocity fields. Thus, the shape of the p.d.f. is significantly wider at lighter-fluid regions than heavier-fluid regions. The dependence on the Atwood number changes during the flow evolution. The velocity field starts to evolve asymmetrically for high- $A$ -number cases, and it tends to lose the  $A$ -number dependence and become symmetric before turbulence decay starts. The density p.d.f. also becomes asymmetric during saturated growth; however, it tends to become symmetric again during gradual decay for the high- $A$ -number cases.

### 6.3. Conditional expectations

Conditional expectations of  $E_{TKE}$ ,  $E_{TKE}$  dissipation and enstrophy were studied to explore the effects of asymmetric behaviour and to study different dynamics of lighter- and heavier-fluid regions. For higher  $A$  numbers, it is shown that all conditional expectations studied here are skewed to the lighter-fluid side, indicating higher  $E_{TKE}$ , dissipation and enstrophy levels within lighter regions. However, again, the dependence on the Atwood number evolves differently for each of the quantities examined. In particular, the conditional expectation of the dissipation becomes  $A$ -number-independent noticeably earlier than the conditional expectation of enstrophy.

### 6.4. Extreme events in HVDT

The local flow statistics were found to exhibit much larger values than their whole-volume averages during both growth regimes. Increasing  $Re_t$  and/or  $A$  numbers increases the probability of the presence of such large deviations from the mean within the flow.

### 6.5. Mixing transition in HVDT

Our results also demonstrate that reaching a high  $Re_t$  number may not be a sufficient condition for achieving mixing transition. The flow has to spend a sufficient time at high  $Re_t$  numbers to become fully developed and undergo a mixing transition. As a result, different metrics attain the mixing transition threshold at different times; the velocity field becomes fully developed substantially earlier than the density field. For example, the velocity p.d.f. reaches its asymptotic behaviour faster than the density p.d.f. and conditional expectations. Moreover, for higher- $A$ -number cases, mixing transition occurs at different times for the different regions of the flow. Thus, mixing transition occurs noticeably earlier within lighter-fluid regions due to more intense turbulence compared to the heavier-fluid regions. In terms of the flow regimes, for the cases with the largest  $Re_t$  and low  $A$ , all investigated quantities reach their fully developed stage during the fast decay everywhere within the flow. However, for the cases with the largest  $Re_t$  and high  $A$ , most of the investigated quantities start to become fully developed in lighter-fluid regions during the saturated growth, whereas for the heavier regions it may take until the end of fast decay to become fully developed.

### 6.6. HVDT spectral evolution

#### 6.6.1. Energy spectra

The dynamic characteristics of HVDT are also reflected in the evolution of the energy spectrum. It is found that the different HVDT regimes have distinctly different

spectral behaviour. The discussion follows using the energy spectrum calculated based on the Favre momentum ( $\rho^* u_i'' / \sqrt{\bar{\rho}}$ ). While the differences are small for the cases considered here, other alternatives such as ( $\sqrt{\bar{\rho}} u_i''$ ) or ( $\sqrt{\bar{\rho}^*} u_i''$ ) cannot be shown to have vanishing viscous effects at very large scales even for constant viscosity, when the  $A$  number is large enough. During explosive growth, when production dominates the intermediate scales, the slope of the energy spectrum is steeper than the classical Kolmogorov spectrum and was found to be close to a  $k^{-7/3}$  power law. During saturated growth, as the energy production-to-dissipation ratio decreases, the slope of the intermediate scales increases from  $-7/3$  to  $-5/3$ . At the end of the growth regimes, production is equal to dissipation and the energy spectrum is similar to the classical Kolmogorov spectrum. During fast decay, as the energy production continues to weaken, its effects are restricted to upper intermediate scales. The scales becomes shallower than a  $k^{-5/3}$  power law. Eventually, during gradual decay, energy spectra remain similar to those at the end of the fast decay regime. Upper intermediate scales, which are affected by energy production, show a  $k^{-1}$  scaling. At lower intermediate scales, a  $k^{-5/3}$  power-law spectrum is recovered for the highest  $Re_0$  examined.

### 6.6.2. Spectral anisotropy

During explosive growth, the normal stresses remain anisotropic at all scales (including inertial and viscous ranges) for all  $Re_t$ - and  $A$ -number cases investigated in this work. During saturated growth, the inertial range isotropy emerges; however, the viscous range continues to be anisotropic. During fast decay, as energy production is lower than dissipation, both inertial and viscous ranges become isotropic. The  $Re_t$  number has a limited effect on the spectral anisotropy during growth regimes. However, higher  $Re_t$  numbers cause faster isotropy emergence at inertial and small scales during the fast decay regime.

### 6.6.3. Density spectra

The density power spectrum normalized by  $(A\bar{\rho})^2$  collapses at large scales for all cases. Since the flow starts from rest, with large heavy- and light-fluid regions, the imprint of these regions on density spectra is relatively slow to vanish. During the fast decay regime, the density spectrum acquires its asymptotic shape and no longer changes as the flow transitions to gradual decay. During this regime, the density spectrum follows a  $k^{-1}$  power law for scales larger than the diffusive scales.

The triply periodic flow configuration removes edge and wall effects and thus allows one to focus on the physics of VD mixing. Compared to classical RTI, HVDT is computationally more efficient and reaches higher Reynolds numbers during flow evolution. HVDT thus allows for exploring VD mixing in regimes further beyond mixing transition. As illustrated, HVDT possesses unique physics that are different from single-fluid turbulence due to different inertia of the light- and heavy-fluid regions. While some of the consequences of this asymmetry, as reflected in joint velocity–density MDFs and conditional expectations, might be obscured in the behaviour of global quantities and energy spectra, they are nevertheless important for the evolution of the flow. Modelling variable-density turbulent flows poses unique challenges in any type of modelling strategy. It is our hope that the higher-Reynolds-number and higher-Atwood-number runs presented here will help in extending turbulence models to capture turbulent flows with large density variations.

**Acknowledgements**

A.B. acknowledges financial support from DOE/NNSA SSAA Program (grant no. DE-NA0003195) and the US National Science Foundation Early CAREER Program (grant no. 1453056 from CBET-Fluid Dynamics). This work is co-authored by an employee of Triad National Security, LLC, which operates Los Alamos National Laboratory under contract no. 89233218CNA000001 with the US Department of Energy/National Nuclear Security Administration. Computational resources were provided by the Institutional Computing Program at Los Alamos National Laboratory and the Argonne Leadership Computing Facility at Argonne National Laboratory through a 2017 ALCC Award.

**Declaration of interests**

The authors report no conflict of interest.

**Appendix A**

To derive a transport equation for the jMDF, we start from the fine-grained, one-point, one-time Eulerian velocity–density j.p.d.f. ( $f_{\rho^*, u_i^*}^*$ ), which is defined by

$$f_{\rho^*, u_i^*}^* = \delta(u_i^* - V_i)\delta(\rho^* - R), \tag{A1}$$

and use the formula  $f_{\rho^*, u_i^*}^* = \langle f_{\rho^*, u_i^*}^* \rangle$ , where  $f_{\rho^*, u_i^*}^*$  is the one-point, one-time Eulerian j.p.d.f. of the velocity and density fields. Also,  $\langle Q(\rho^*, u_i^*)f_{\rho^*, u_i^*}^* \rangle = \langle Q(\rho^*, u_i^*)|_{V_i, R} \rangle$  is the conditional expectation of any function  $Q(\rho^*, u_i^*; x_i, t)$  at  $u_i^* = V_i$  and  $\rho^* = R$ . For a homogeneous flow, averages are constant in space.

Then, the transport equation for  $f_{\rho^*, u_i^*}^*$  can be derived by explicitly calculating the material derivative:

$$\rho^* \frac{Df_{\rho^*, u_i^*}^*}{Dt} = \rho^* \frac{\partial f_{\rho^*, u_i^*}^*}{\partial t} + \rho^* u_j^* \frac{\partial f_{\rho^*, u_i^*}^*}{\partial x_j}, \tag{A2}$$

using the chain rule

$$\frac{\partial f_{\rho^*, u_i^*}^*}{\partial t} = - \frac{\partial f_{\rho^*, u_i^*}^*}{\partial V_j} \frac{\partial u_j^*}{\partial t} - \frac{\partial f_{\rho^*, u_i^*}^*}{\partial R} \frac{\partial \rho^*}{\partial t} \tag{A3}$$

and

$$\frac{\partial f_{\rho^*, u_i^*}^*}{\partial x_i} = - \frac{\partial f_{\rho^*, u_i^*}^*}{\partial V_j} \frac{\partial u_j^*}{\partial x_i} - \frac{\partial f_{\rho^*, u_i^*}^*}{\partial R} \frac{\partial \rho^*}{\partial x_i}. \tag{A4}$$

By using (A3) and (A4), the transport equation can be written as

$$\begin{aligned} \rho^* \frac{\partial f_{\rho^*, u_i^*}^*}{\partial t} + \rho^* u_j^* \frac{\partial f_{\rho^*, u_i^*}^*}{\partial x_j} &= -\rho^* \frac{\partial f_{\rho^*, u_i^*}^*}{\partial V_j} \frac{\partial u_j^*}{\partial t} - \rho^* u_i^* \frac{\partial f_{\rho^*, u_i^*}^*}{\partial V_j} \frac{\partial u_j^*}{\partial x_i} \\ &\quad - \rho^* \frac{\partial f_{\rho^*, u_i^*}^*}{\partial R} \frac{\partial \rho^*}{\partial t} - \rho^* u_i^* \frac{\partial f_{\rho^*, u_i^*}^*}{\partial R} \frac{\partial \rho^*}{\partial x_i} \\ &= -\frac{\partial}{\partial V_j} \left[ \rho^* \left( \frac{\partial u_j^*}{\partial t} + u_i^* \frac{\partial u_j^*}{\partial x_i} \right) f_{\rho^*, u_i^*}^* \right] \end{aligned}$$

$$\begin{aligned}
 & -\frac{\partial}{\partial R} \left[ \rho^* \left( \frac{\partial \rho^*}{\partial t} + u_i^* \frac{\partial \rho^*}{\partial x_i} \right) f_{\rho^*, u_i^*}^* \right] \\
 & = -\frac{\partial}{\partial V_j} \left[ \rho^* \frac{D u_j^*}{D t} f_{\rho^*, u_i^*}^* \right] - \frac{\partial}{\partial R} \left[ \rho^* \frac{D \rho^*}{D t} f_{\rho^*, u_i^*}^* \right]. \tag{A5}
 \end{aligned}$$

By using the continuity equation, the left-hand side of equation (A5) becomes  $\partial(\rho^* f_{\rho^*, u_i^*}^*)/\partial t + \partial(\rho^* u_j^* f_{\rho^*, u_i^*}^*)/\partial x_j$ . After taking the average and using the sifting property of the delta function, such that  $\rho^*$  can be replaced by  $R$  and  $u_i^*$  by  $V_i$ , equation (A5) turns into

$$\frac{\partial(R f_{\rho^*, u_i^*}^*)}{\partial t} + \frac{\partial(R V_j f_{\rho^*, u_i^*}^*)}{\partial x_j} = -\frac{\partial}{\partial V_i} \left[ R f_{\rho^*, u_i^*}^* \left\langle \frac{D u_i^*}{D t} \right\rangle \Big|_{V_i, R} \right] - \frac{\partial}{\partial R} \left[ R f_{\rho^*, u_i^*}^* \left\langle \frac{D \rho^*}{D t} \right\rangle \Big|_{V_i, R} \right]. \tag{A6}$$

Using the relation between the j.p.d.f. and MDF, which for homogeneous flows becomes  $\mathcal{F}_{u_i \rho^*}(V_i, R; t) = \mathcal{F} = R f_{u_i \rho^*}(V_i, R; t)$ , the equation turns into

$$\frac{\partial \mathcal{F}}{\partial t} = -\frac{\partial}{\partial V_i} \left[ \mathcal{F} \left\langle \frac{D u_i^*}{D t} \right\rangle \Big|_{V_i, R} \right] - \frac{\partial}{\partial R} \left[ \mathcal{F} \left\langle \frac{D \rho^*}{D t} \right\rangle \Big|_{V_i, R} \right]. \tag{A7}$$

Finally, from (2.1) and (2.2) the material derivatives of the density and velocity fields can be written as

$$\frac{D \rho^*}{D t} = \rho_{,i}^* + \rho_j^* u_j^* = -\rho^* u_{j,j}^*, \tag{A8}$$

$$\frac{D u_i^*}{D t} = (u_i^*)_{,i} + u_j^* u_{i,j}^* = -\frac{1}{\rho^*} (p_{,i} + P_{,i} - \tau_{ij,j}^*) + \frac{1}{Fr^2} g_i. \tag{A9}$$

Upon combining (A7)–(A9), the final version of the transport equation of  $\mathcal{F}$  can be written as

$$\begin{aligned}
 \frac{d \mathcal{F}}{d t} + \frac{d V_j \mathcal{F}}{d x_j} & = -\frac{\partial}{\partial V_i} \left[ \mathcal{F} \left\langle -\frac{p_{,i}}{\rho^*} \Big|_{V_i, R} - \frac{P_{,i}}{\rho^*} \Big|_{V_i, R} + \frac{\tau_{ij,j}^*}{\rho^*} \Big|_{V_i, R} + \frac{1}{Fr^2} g_i \Big|_{V_i, R} \right\rangle \right] \\
 & - \frac{\partial}{\partial R} [\mathcal{F} \langle -\rho^* u_{j,j}^* |_{V_i, R} \rangle]. \tag{A10}
 \end{aligned}$$

REFERENCES

ADKINS, J. F., MCINTYRE, K. & SCHRAG, D. P. 2002 The salinity, temperature, and  $\delta^{18}O$  of the glacial deep ocean. *Science* **298** (5599), 1769–1773.

AHLERS, G., GROSSMANN, S. & LOHSE, D. 2009 Heat transfer and large scale dynamics in turbulent Rayleigh–Bénard convection. *Rev. Mod. Phys.* **81**, 503–537.

AKULA, B. & RANJAN, D. 2016 Dynamics of buoyancy-driven flows at moderately high Atwood numbers. *J. Fluid Mech.* **795**, 313–355.

ALMAGRO, A., GARCÍA-VILLALBA, M. & FLORES, O. 2017 A numerical study of a variable-density low-speed turbulent mixing layer. *J. Fluid Mech.* **830**, 569–601.

ASLANGIL, D., BANERJEE, A. & LAWRIE, A. G. W. 2016 Numerical investigation of initial condition effects on Rayleigh–Taylor instability with acceleration reversals. *Phys. Rev. E* **94**, 053114.

- ASLANGIL, D., LIVESCU, D. & BANERJEE, A. 2019 Flow regimes in buoyancy-driven homogeneous variable-density turbulence. In *Progress in Turbulence VIII* (ed. R. Örlü, A. Talamelli, J. Peinke & M. Oberlack), pp. 235–240. Springer International Publishing.
- ASLANGIL, D., LIVESCU, D. & BANERJEE, A. 2020 Variable-density buoyancy-driven turbulence with asymmetric initial density distribution. *Physica D* **406**, 132444.
- BAILIE, C., MCFARLAND, J. A., GREENOUGH, J. A. & RANJAN, D. 2012 Effect of incident shock wave strength on the decay of Richtmyer–Meshkov instability-introduced perturbations in the refracted shock wave. *Shock Waves* **22** (6), 511–519.
- BALTZER, J. R. & LIVESCU, D. 2020 Variable-density effects in incompressible non-buoyant shear-driven turbulent mixing layers. *J. Fluid Mech.* (under review).
- BANERJEE, A. & ANDREWS, M. J. 2009 3D Simulations to investigate initial condition effects on the growth of Rayleigh–Taylor mixing. *Intl J. Heat Mass Transfer* **52** (17), 3906–3917; special Issue Honoring Professor D. Brian Spalding.
- BANERJEE, A., KRAFT, W. N. & ANDREWS, M. J. 2010 Detailed measurements of a statistically steady Rayleigh–Taylor mixing layer from small to high Atwood numbers. *J. Fluid Mech.* **659**, 127–190.
- BATCHELOR, G. K., CANUTO, V. M. & CHASNOV, J. R. 1992 Homogeneous buoyancy-generated turbulence. *J. Fluid Mech.* **235**, 349–378.
- BROUILLETTE, M. 2002 The Richtmyer–Meshkov Instability. *Annu. Rev. Fluid Mech.* **34** (1), 445–468.
- CABOT, W. & COOK, A. 2006 Reynolds number effects on Rayleigh–Taylor instability with possible implications for type Ia supernovae. *Nat. Phys.* **2**, 562–568.
- CHARONKO, J. J. & PRESTRIDGE, K. 2017 Variable-density mixing in turbulent jets with coflow. *J. Fluid Mech.* **825**, 887–921.
- CHUNG, D. & PULLIN, D. I. 2010 Direct numerical simulation and large-eddy simulation of stationary buoyancy-driven turbulence. *J. Fluid Mech.* **643**, 279–308.
- CLARK, T. T. & SPITZ, P. B. 2005 Two-point correlation equations for variable density turbulence. *Tech. Rep.* LA-12671-MS. Los Alamos Technical Report.
- CLEMENS, N. T. & MUNGAL, M. G. 1995 Large-scale structure and entrainment in the supersonic mixing layer. *J. Fluid Mech.* **284**, 171–216.
- COLGATE, S. A. & WHITE, R. H. 1966 The hydrodynamic behavior of supernovae explosions. *Astrophys. J.* **143**, 626–681.
- COOK, A. W. & DIMOTAKIS, P. E. 2001 Transition stages of Rayleigh–Taylor instability between miscible fluids. *J. Fluid Mech.* **443**, 69–99.
- COOK, A. W. & ZHOU, Y. 2002 Energy transfer in Rayleigh–Taylor instability. *Phys. Rev. E* **66**, 026312.
- DANIEL, D., LIVESCU, D. & RYU, J. 2018 Reaction analogy based forcing for incompressible scalar turbulence. *Phys. Rev. Fluids* **3**, 094602.
- DIMONTE, G. & SCHNEIDER, M. 1996 Turbulent Rayleigh–Taylor instability experiments with variable acceleration. *Phys. Rev. E* **54**, 3740–3743.
- DIMONTE, G., YOUNGS, D. L., DIMITS, A., WEBER, S., MARINAK, M., WUNSCH, S., GARASI, C., ROBINSON, A., ANDREWS, M. J., RAMAPRABHU, P. *et al.* 2004 A comparative study of the turbulent Rayleigh–Taylor instability using high-resolution three-dimensional numerical simulations: The alpha-group collaboration. *Phys. Fluids* **16** (5), 1668–1693.
- DIMOTAKIS, P. E. 2000 The mixing transition in turbulent flows. *J. Fluid Mech.* **409**, 69–98.
- GAT, I., MATHEOU, G., CHUNG, D. & DIMOTAKIS, P. E. 2017 Incompressible variable-density turbulence in an external acceleration field. *J. Fluid Mech.* **827**, 506–535.
- GETLING, A. V. 1998 *Rayleigh–Beñard Convection*. World Scientific.
- GIVI, P. 1989 Model-free simulations of turbulent reactive flows. *Prog. Energy Combust. Sci.* **15** (1), 1–107.
- GULL, S. F. 1975 The x-ray, optical and radio properties of young supernova remnants. *Mon. Not. R. Astron. Soc.* **171** (2), 263–278.
- HAWORTH, D. C. 2010 Progress in probability density function methods for turbulent reacting flows. *Prog. Energy Combust. Sci.* **36** (2), 168–259.

- KIDA, S. & ORSZAG, S. A. 1990 Energy and spectral dynamics in forced compressible turbulence. *J. Sci. Comput.* **5**, 85–125.
- KLIMENKO, A. Y. & POPE, S. B. 2003 The modeling of turbulent reactive flows based on multiple mapping conditioning. *Phys. Fluids* **15** (7), 1907–1925.
- KOLLA, H., ROGERSON, J. W., CHAKRABORTY, N. & SWAMINATHAN, N. 2009 Scalar dissipation rate modeling and its validation. *Combust. Sci. Technol.* **181** (3), 518–535.
- LAI, C. C. K., CHARONKO, J. J. & PRESTRIDGE, K. P. 2018 A Karman–Howarth–Monin equation for variable-density turbulence. *J. Fluid Mech.* **843**, 382–418.
- LESIEUR, M. & ROGALLO, R. 1989 Large-eddy simulation of passive scalar diffusion in isotropic turbulence. *Phys. Fluids A* **1** (4), 718–722.
- LINDEN, P. F., REDONDO, J. M. & YOUNGS, D. L. 1994 Molecular mixing in Rayleigh–Taylor instability. *J. Fluid Mech.* **265**, 97–124.
- LINDL, J. 1995 Development of the indirect-drive approach to inertial confinement fusion and the target physics basis for ignition and gain. *Phys. Plasmas* **2** (11), 3933–4024.
- LINDL, J. D. 1998 *Inertial Confinement Fusion: The Quest for Ignition and Energy Gain Using Indirect Drive*. AIP Press.
- LIVESCU, D. 2013 Numerical simulations of two-fluid turbulent mixing at large density ratios and applications to the Rayleigh–Taylor instability. *Phil. Trans. R. Soc. Lond. A* **371**, 20120185.
- LIVESCU, D. 2020 Turbulence with large thermal and compositional density variations. *Annu. Rev. Fluid Mech.* **52**, 309–341.
- LIVESCU, D., CANADA, C., KANOV, K., BURNS, R., IDIES STAFF & PULIDO, J. 2014 Homogeneous buoyancy driven turbulence dataset. Available at <http://turbulence.pha.jhu.edu/docs/README-HBDT.pdf>.
- LIVESCU, D., JABERI, F. A. & MADNIA, C. K. 2000 Passive-scalar wake behind a line source in grid turbulence. *J. Fluid Mech.* **416**, 117–149.
- LIVESCU, D. & RISTORCELLI, J. R. 2007 Buoyancy-driven variable-density turbulence. *J. Fluid Mech.* **591**, 43–71.
- LIVESCU, D. & RISTORCELLI, J. R. 2008 Variable-density mixing in buoyancy-driven turbulence. *J. Fluid Mech.* **605**, 145–180.
- LIVESCU, D. & RISTORCELLI, J. R. 2009 Mixing asymmetry in variable density turbulence. In *Advances in Turbulence XII* (ed. B. Eckhardt), vol. 132, pp. 545–548. Springer.
- LIVESCU, D., RISTORCELLI, J. R., GORE, R. A., DEAN, S. H., CABOT, W. H. & COOK, A. W. 2009 High-Reynolds number Rayleigh–Taylor turbulence. *J. Turbul.* **10**, N13.
- LIVESCU, D., RISTORCELLI, J. R., PETERSEN, M. R. & GORE, R. A. 2010 New phenomena in variable-density Rayleigh–Taylor turbulence. *Phys. Scr.* **2010** (T142), 014015.
- LIVESCU, D. & WEI, T. 2012 Direct numerical simulations of Rayleigh–Taylor instability with gravity reversal. In *Proceedings of the Seventh International Conference on Computational Fluid Dynamics (ICCFD7), Big Island, HI, July 9–13, 2012*, p. 2304.
- LIVESCU, D., WEI, T. & PETERSEN, M. R. 2011 Direct numerical simulations of Rayleigh–Taylor instability. *J. Phys.: Conf. Ser.* **318** (8), 082007.
- LUMLEY, J. L. 1967 Similarity and the turbulent energy spectrum. *Phys. Fluids* **10** (4), 855–858.
- MESHKOV, E. E. 1969 Instability of the interface of two gases accelerated by a shock wave. *Fluid Dyn.* **4** (5), 101–104.
- MOLCHANOV, O. A. 2004 On the origin of low- and middle-latitude ionospheric turbulence. *Phys. Chem. Earth A/B/C* **29** (4), 559–567; seismo Electromagnetics and Related Phenomena.
- NAKAI, S. & MIMA, K. 2004 Laser driven inertial fusion energy: present and prospective. *Rep. Prog. Phys.* **67** (3), 321.
- NAKAI, S. & TAKABE, H. 1996 Principles of inertial confinement fusion – physics of implosion and the concept of inertial fusion energy. *Rep. Prog. Phys.* **59** (9), 1071.
- NISHIHARA, K., WOUCHUK, J. G., MATSUOKA, C., ISHIZAKI, R. & ZHAKHOVSKY, V. V. 2010 Richtmyer–Meshkov instability: theory of linear and nonlinear evolution. *Phil. Trans. R. Soc. Lond. A* **368** (1916), 1769–1807.
- NOURI, A. G., GIVI, P. & LIVESCU, D. 2019 Modeling and simulation of turbulent nuclear flames in type Ia supernovae. *Prog. Aerosp. Sci.* **108**, 156–179.

- OVERHOLT, M. R. & POPE, S. B. 1996 Direct numerical simulation of a passive scalar with imposed mean gradient in isotropic turbulence. *Phys. Fluids* **8** (11), 3128–3148.
- PAL, N., KURIEN, S., CLARK, T. T., ASLANGIL, D. & LIVESCU, D. 2018 Two-point spectral model for variable-density homogeneous turbulence. *Phys. Rev. Fluids* **3**, 124608.
- POPE, S. B. 1985 PDF methods for turbulent reactive flows. *Prog. Energy Combust. Sci.* **11** (2), 119–192.
- POPE, S. B. 2000 *Turbulent Flows*. Cambridge University Press.
- RAMAPRABHU, P., KARKHANIS, V. & LAWRIE, A. G. W. 2013 The Rayleigh–Taylor Instability driven by an accel-decel-accel profile. *Phys. Fluids* **25** (11), 115104.
- RAO, P., CAULFIELD, C. P. & GIBBON, J. D. 2017 Nonlinear effects in buoyancy-driven variable-density turbulence. *J. Fluid Mech.* **810**, 362–377.
- RAYLEIGH, LORD 1884 Investigation of the character of the equilibrium of an incompressible heavy fluid of variable density. *Proc. Lond. Math. Soc.* **s1-14** (1), 170–177.
- RICHTMYER, R. D. 1960 Taylor instability in shock acceleration of compressible fluids. *Commun. Pure Appl. Maths* **13** (2), 297–319.
- RISTORCELLI, J. R. & CLARK, T. T. 2004 Rayleigh–Taylor turbulence: self-similar analysis and direct numerical simulations. *J. Fluid Mech.* **507**, 213–253.
- SANDOVAL, D. L. 1995 The dynamics of variable density turbulence. PhD thesis, University of Washington.
- SANDOVAL, D. L., CLARK, T. T. & RILEY, J. J. 1997 Buoyancy-generated variable-density turbulence. In *IUTAM Symposium on Variable Density Low-Speed Turbulent Flows: Proceedings of the IUTAM Symposium held in Marseille, France, 8–10 July 1996* (ed. L. Fulachier, J. L. Lumley & F. Anselmet), pp. 173–180. Springer Netherlands.
- SCHILLING, O. & LATINI, M. 2010 High-order WENO simulations of three-dimensional reshocked Richtmyer–Meshkov instability to late times: dynamics, dependence on initial conditions, and comparisons to experimental data. *Acta Mathematica Scientia* **30** (2), 595–620; Mathematics dedicated to professor James Glimm on the occasion of his 75th birthday.
- SCHILLING, O., LATINI, M. & DON, W. S. 2007 Physics of reshock and mixing in single-mode Richtmyer–Meshkov instability. *Phys. Rev. E* **76**, 026319.
- SCHWARZKOPF, J. D., LIVESCU, D., BALTZER, J. R., GORE, R. A. & RISTORCELLI, J. R. 2016 A two-length scale turbulence model for single-phase multi-fluid mixing. *Flow Turbul. Combust.* **96**, 1–43.
- SELLERS, C. L. & CHANDRA, S. 1997 Compressibility effects in modelling turbulent high speed mixing layers. *Engng Comput.* **14** (1), 5–13.
- SOULARD, O. & GRIFFOND, J. 2012 Inertial-range anisotropy in Rayleigh–Taylor turbulence. *Phys. Fluids* **24**, 025101.
- TAYLOR, G. I. 1950 The instability of liquid surfaces when accelerated in a direction perpendicular to their planes. I. *Proc. R. Soc. Lond. A* **201** (1065), 192–196.
- WUNSCH, C. & FERRARI, R. 2004 Vertical mixing, energy, and the general circulation of the oceans. *Annu. Rev. Fluid Mech.* **36** (1), 281–314.
- YOUNGS, D. L. 1991 Three-dimensional numerical simulation of turbulent mixing by Rayleigh–Taylor instability. *Phys. Fluids A* **3** (5), 1312–1320.
- ZHAO, D. & ALUIE, H. 2018 Inviscid criterion for decomposing scales. *Phys. Rev. Fluids* **3**, 054603.
- ZHOU, Y. 2017a Rayleigh–Taylor and Richtmyer–Meshkov instability induced flow, turbulence, and mixing. I. *Phys. Rep.* **720–722**, 1–136.
- ZHOU, Y. 2017b Rayleigh–Taylor and Richtmyer–Meshkov instability induced flow, turbulence, and mixing. II. *Phys. Rep.* **723–725**, 1–160.